

# Scanning Acoustic Microscopy for Quantifying Two-phase Transfer in *Operando* Alkaline Water Electrolyzer

Zehua Dou <sup>1,7,\*</sup>, Hannes Rox <sup>2</sup>, Zyzi Ramos <sup>3</sup>, Robert Baumann <sup>4</sup>, Rachappa Ravishankar <sup>8</sup>, Peter Czurratis <sup>3</sup>, Xuegeng Yang <sup>2</sup>, Andrés Fabian Lasagni <sup>4,5</sup>, Kerstin Eckert <sup>2,6,7</sup>, Juergen Czarske <sup>1</sup> and David Weik <sup>1</sup>

<sup>1</sup> Faculty of Electrical and Computer Engineering, Laboratory of Measurement and Sensor System Technique, Technische Universität Dresden, Helmholtzstraße 18, 01069 Dresden, Germany

<sup>2</sup> Institute of Fluid Dynamics, Helmholtz-Zentrum Dresden-Rossendorf, Bautzner Landstraße 400, 01328 Dresden, Germany

<sup>3</sup> PVA TePla Analytical Systems GmbH, Deutschordenstraße 38, 73463 Westhausen, Germany

<sup>4</sup> Institute of Manufacturing Science and Engineering, Technische Universität Dresden, George-Baehr-Straße 3c, 01069 Dresden, Germany

<sup>5</sup> Fraunhofer Institute for Material and Beam Technology IWS, Winterbergstraße 28, 01277 Dresden, Germany

<sup>6</sup> Institute of Process Engineering and Environmental Technology, Technische Universität Dresden, Helmholtzstraße 14, 01069 Dresden, Germany

<sup>7</sup> Hydrogen Lab, School of Engineering, Technische Universität Dresden, Helmholtzstraße 14, 01062 Dresden, Germany

<sup>8</sup> Institute for Emerging Electronic Technologies, Leibniz Institute for Solid State and Materials Research Dresden, Helmholtzstraße 20, 01069 Dresden, Germany

\* zehua.dou@tu-dresden.de

## ABSTRACT

Improved understandings of two-phase transport in electrochemical gas-evolving systems are increasingly demanded, while high-performance imaging techniques using simplified instrumentations are not readily available. This work presents volumetric scanning acoustic microscopy (SAM) imaging for quantifying the dynamics of gas bubbles and electrolyte in porous Nickel electrodes with different wettability and structures during alkaline water electrolysis (AWE). We realize high-resolution 3D imaging at 10's  $\mu\text{m}$  level using high frequency spherically focused ultrasound. The high resolution allowed us to clearly visualize the spatial distributions of produced bubbles in the porous electrodes over time. Moreover, we are able to quantify the residual gas volume in an electrode and its coverage due to bubble evolution, which dominate its transport overpotential. Taking these advantages, we elucidate the impacts of electrodes' wettability and structures on their electrolysis performance, on a regular laboratory base. The obtained knowledge provides us important optimization guidelines of AWE designs and operating schemes.

**Keywords:** green hydrogen energy, scanning acoustic microscopy, volumetric ultrasound imaging, alkaline water electrolysis, mass transfer, two-phase flow, gas evolving electrode, bubble management.

## 1. INTRODUCTION

Low temperature water electrolysis technologies, namely alkaline water electrolyzers (AWEs) and proton exchange membrane water electrolyzers (PEMWEs), show great potential for producing green hydrogen ( $H_2$ ) at large scale, and preventing for the global warming crisis.<sup>1,2</sup> In comparison with PEMWEs that rely on noble metals,<sup>3</sup> transition metals based AWEs possess competitive capital costs but suffer from low production rate featured by low current densities. The current density of an AWE is typically in the range of 100 – 500 mA/cm<sup>2</sup>,<sup>4</sup> which is inferior than the value of 600 – 3000 mA/cm<sup>2</sup> that can be reached by PEMWEs at comparable cell voltages.<sup>5</sup> It is nowadays accepted that the transport overpotential dominated by the two-phase (gas and electrolyte) mass transfer presents one of the major challenges for realizing high  $H_2$  production rate of AWE.<sup>6,7</sup> Therefore, innovative AWE designs that enable superior bubble removal and electrolyte replenishments are crucial to increase their productivity towards facilitating the transition to cost competitive green  $H_2$  energy.<sup>8</sup> To date, optimizing porous electrodes,<sup>9–11</sup> flow field designs,<sup>12,13</sup> and control schemes have been demonstrated for achieving outstanding AWE current densities beyond 1000 mA/cm<sup>2</sup> at low cell voltages.<sup>14</sup> However, the best combinations of these strategies realizing the optimal AWE performance for certain applications mostly remain unclear.<sup>15,16</sup> To fill this research gap, imaging techniques that are able to quantify the two-phase transport in AWEs in their practical operating environment and conditions are highly demanded to obtain optimization guidelines.<sup>17,18</sup>

Up to date, extended understandings on two-phase flow in electrolyzers obtained by optical imaging, synchrotron X-ray and neutron radiography and computed tomography (CT) have gained tremendous attention.<sup>8</sup> Direct visualizations with high speed cameras, on one hand, present a straightforward approach for real-time quantifications of e.g., electrode coverage due to bubble evolution and bubble size distribution in opened electrolysis systems and transparently designed test AWEs.<sup>19–21</sup> However, optical imaging systems are incapable of investigating bubble dynamics inside optically opaque porous electrodes. Synchrotron X-rays and neutrons, on the other hand, are able to deeply penetrate electrolyzer components. Advanced CT instrumentations based on modern high flux beamlines show great potential to achieve 3D imaging in real-time with micrometer level spatial resolutions.<sup>22,23</sup> Taking these advantages, synchrotron X-ray and neutron imaging haven been extensively performed in PEMWE related studies,<sup>24–28</sup> and a few investigations of AWEs were reported as well.<sup>29,30</sup> However, these imaging systems usually possess adequate phase contrast to fully render the two-phase flow behaviours in technical relevant electrodes. Specifically, X-rays are highly attenuated in metallic materials e.g., Titanium (Ti) based porous transport layers (PTL) of PEMWEs, which results to poor gas/liquid contrast.<sup>26,27</sup> On the contrary, neutrons are strongly attenuated by water, which leads to the metallic electrodes undistinguished from the produced gas bubbles.<sup>31,32</sup> Such limitations are likely to persist in AWEs related studies, as the attenuation coefficients of X-rays and neutrons in AWE electrode materials e.g., Nickel (Ni) are similar to the aforementioned values of the Ti-PTL in PEMWEs.<sup>33,34</sup> Although the contrast issue can be solved by introducing contrast agents or combined X-ray and neutron imaging schemes,<sup>31,35</sup> the complicated and costly instrumentations, as well as the limited access to the beamlines may drastically hinder the laboratory-based research work flows.

Ultrasonic imaging techniques recently open new horizons to study two-phase transport in electrolyzers using cost-effective instrumentations with the potential to omit the phase contrast issues. M. Maier *et al.* reported a pulse-echo ultrasonic imaging of *operando* PEMWEs using a 5 MHz linear ultrasonic transducer array.<sup>36</sup> Due to the drastically different acoustic impedances among the metallic electrodes, gas bubbles and water, the flow field, porous electrode and gas contents in the flow channels were clearly distinguished. However, the realized spatial resolution was only 1 mm, which prevents the detailed visualizations of two-phase flow behaviours within the porous electrode. This is because the low frequency liner transducer array possesses a lack of ability to focus the ultrasound properly. In theory,

the lateral resolution of an ultrasonic imaging system is defined by the ultrasound beam diameter of the employed ultrasonic transducer, which is calculated as the ultrasound wavelength divided by the transducer's angular aperture.<sup>37</sup> While its axial resolution corresponds to the propagation length of the excited ultrasound pulses in the imaging environment.<sup>38</sup> To sum up, ultrasound imaging with high resolution of 10's  $\mu\text{m}$  level requires high frequency transducers e.g., above 50 MHz and spherical focusing acoustic lens with large angular apertures. One implementation of such an instrumentation is known as scanning acoustic microscopy (SAM) that is able to provide a spatial resolution up to sub-micrometer in opaque materials. Taking these advantages, SAM has found extensive applications in non-destructive evaluations for material researches and the semiconductor industry,<sup>39,40</sup> characterizations of biological tissues,<sup>41</sup> and it has nowadays emerged as an efficient approach to study the degradations of Lithium-ion batteries.<sup>42</sup> Such a powerful tool thus shows tremendous potential to make a breakthrough advancing the developments of low temperature electrolyzers, supplementing to the costly and complicated X-ray and neutron based imaging methods.

In this work, we experimentally validate the feasibility of quantifying the two-phase flow behaviours in *operando* AWEs performing volumetric SAM imaging. To demonstrate the general applicability of this imaging technique, we investigate Ni woven mesh and open cell Ni foam electrodes that are representative for a wide range of technical relevant AWE electrodes. Moreover, the influences of electrodes' wettability to their transport properties and electrolysis performance are also explored. For this, we use a laser texturing technique to adjust the wettability of the two types of electrodes from hydrophobic (before texturing) to wicking (after). The two-phase flows behaviours in these electrodes are individually investigated in a bespoke AWE at various operating conditions. Meanwhile, volumetric images of the electrodes during the hydrogen evolution reaction (HER) are acquired with a leading-edge SAM system, providing a lateral resolution of 70  $\mu\text{m}$  and an axial resolution of 10  $\mu\text{m}$ . In order to understand the mechanisms of the electrodes' wettability and structures influenced their HER performance, we quantify the volumes of entrapped gas bubbles in these electrodes and the electrodes' coverages during electrolysis. Such quantitative analysis provides us important insights to optimize the electrode configurations, flow field designs and operating schemes for overcoming the transport limitations, towards AWEs with higher efficiencies and productivity.

## 2. RESULTS AND DISCUSSIONS

### 2.1 Characterizations of Ni mesh and Ni foam electrodes

In the experiments, in total four different electrodes were investigated, including two pure Ni woven mesh (NM) electrodes and two open cell Ni foam (NF) electrodes, with a same dimension of  $30 \times 10 \text{ mm}^2$ . The thicknesses of NM and NF were 140  $\mu\text{m}$  and 1.5 mm, respectively. Moreover, the NM possessed a wire diameter of 140  $\mu\text{m}$  and a pore size of 500  $\mu\text{m}$  (**Figure 1A & B**). While, the NF present a porosity of approx. 94% and a pore diameter of approx. 200  $\mu\text{m}$  (**Figure 1C & D**). In order to investigate the influences of electrodes' wettability to their transport properties, the surfaces of one NM and one NF were textured using direct laser writing (DLW) technique (see the experimental section for the detailed fabrication process and parameters). One of the biggest advantages of this method is the ability to adjust the surface wettability without relying on specific electrocatalytic nanostructure.<sup>43</sup> The laser induces grooves are clearly observed from the SEM images of the textured NM and NF (see the right column of **Figure 1B & D**), and they are thereafter named as LNM and LNF, respectively. These grooves effectively increased the surface roughness of the electrodes and therefore amplified the intrinsic hydrophilicity of local Ni surface.<sup>44</sup> This resulted to the transitions of the electrodes' wetting states from the Cassie-Baxter state hydrophobic before texturing to the wicking states after texturing,<sup>45</sup> which is indicated by the apparent contact angles of the four electrodes shown in **Figure 1E - F**.

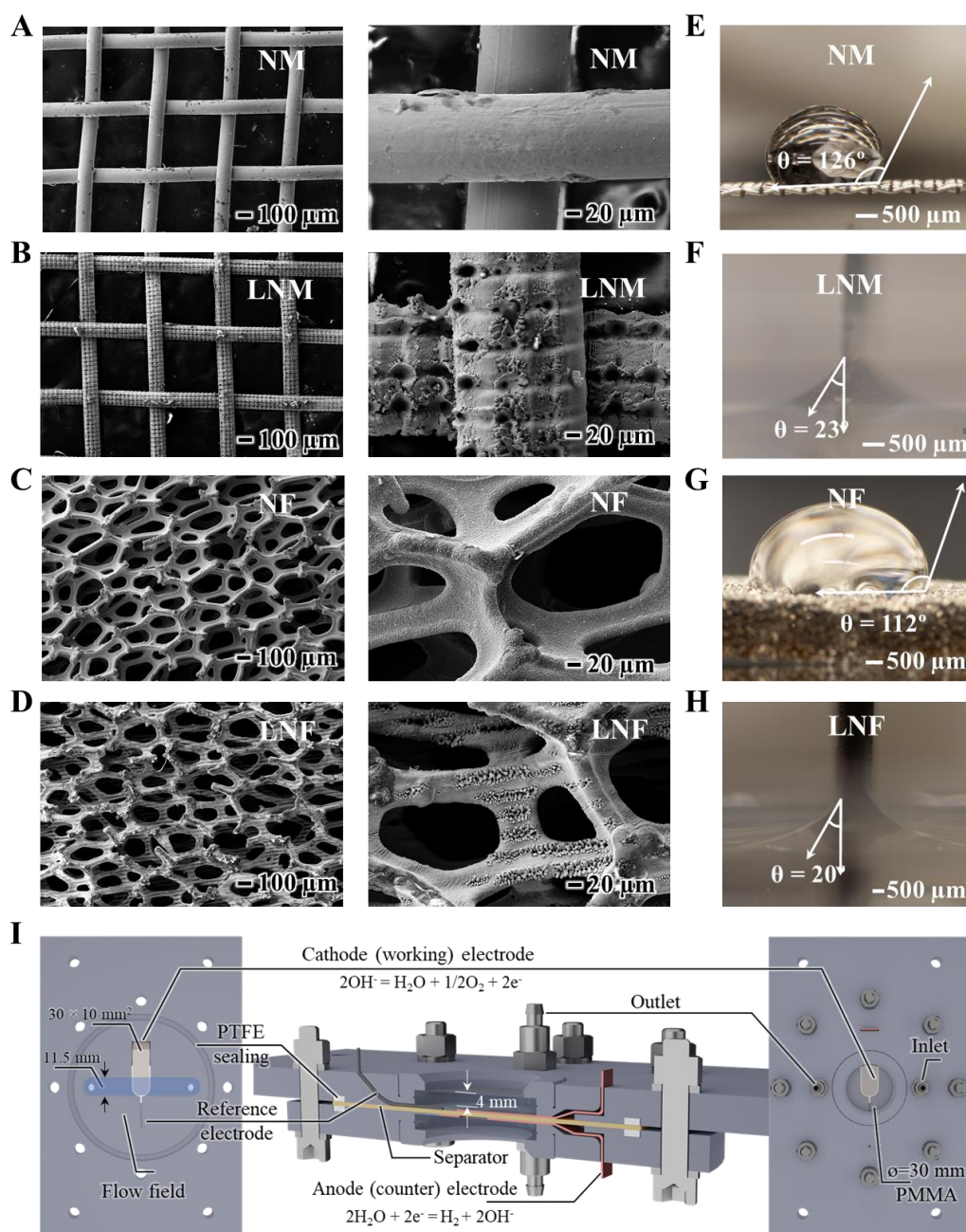


**Figure 1. The four investigated electrodes and the bespoke zero-gap flow-by AWE.**

(A) - (D) The SEM images of the four electrodes: (A) NM, (B) LNM, (C) NF and (D) LNF. The left and right columns show their images with low and high magnifications, respectively. The laser induced grooves only appear on the surfaces of the two textured electrodes i.e., the LNM and LNF but not on their untextured counterparts.

(E) – (H) The apparent contact angles of the four electrodes: (E) NM, (F) LNM, (G) NF and (H) LNF.

(I) A schematic diagram of the bespoke zero-gap flow-by AWE, which depicts its structure, geometry and flow field design. The blue shade represents the single straight flow channel.

To investigate the HER performance of the four electrodes closer to their practical application environment, a miniaturised zero-gap flow-by AWE was in-house developed, as shown in **Figure 1I** (also see **Figure S1** for the pictures showing the parts). The single straight flow channel allowed the electrolyte to flow in parallel with the electrode surface (blue shade **Figure 1I**), which is referred as a flow-by condition. In the flow field, the channel width of 11.5 mm partially overlaid with the investigated electrodes in the cathode, and the rest section of the electrodes out of the flow channel was thus analogue to the case of under a rib.<sup>27,35</sup> Due to the space constrictions in the test AWE, a Pt wire

was used here as a pseudo RE (PRE), as suggested in.<sup>46</sup> At the anode side, a ring shape NM served as the counter electrode (see **Figure S1**) constructing a closed electrical circuit. A separator was placed between the anode and cathode to avoid short circuit and gas crossover.

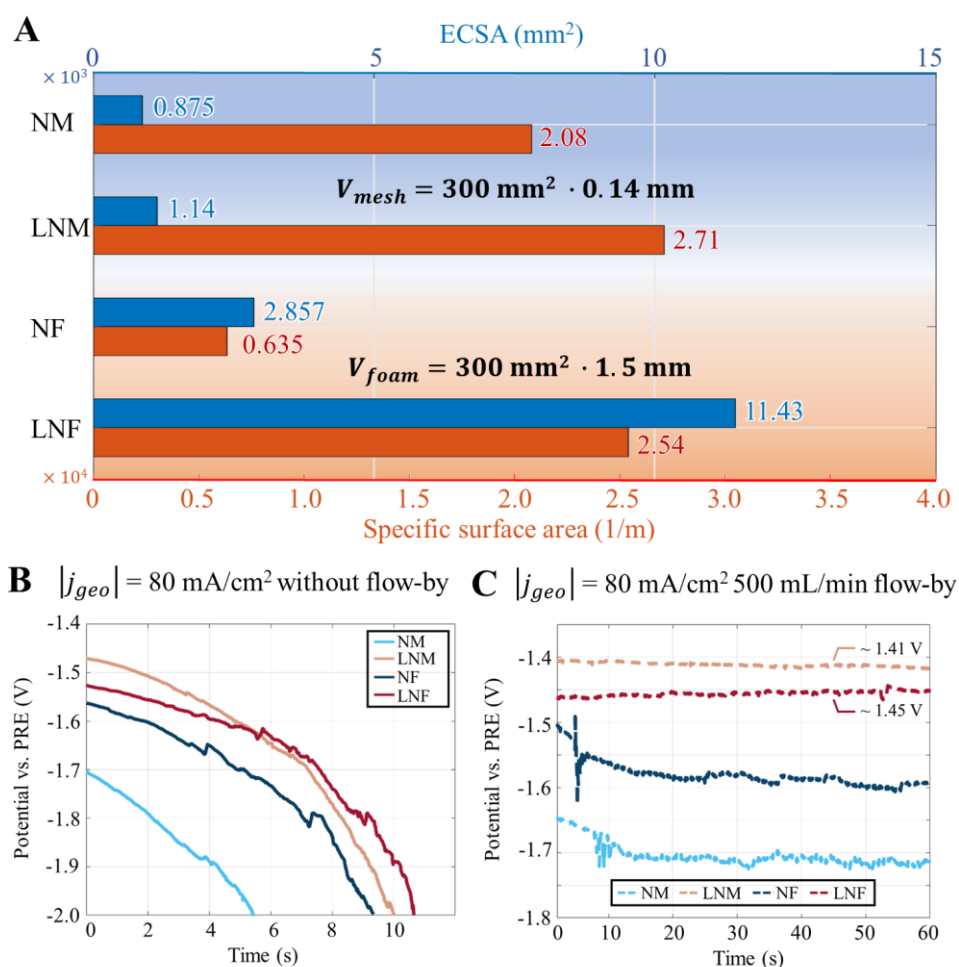


**Figure 2. Electrochemical characterizations of the four electrodes.**

(A) The ECSAs and specific surface areas of the four electrodes, in which the volumes of the NM and NF for calculating the specific surface areas are given. The enhanced wetting and surface roughness enlarged the ECSAs and specific surface areas of LNM and LNF.

(B) - (C) The potential curves collected during galvanostatic electrolysis of the four electrodes for HER, at a geometrical current density of 80 mA/cm<sup>2</sup>, with (B) and without (C) applying a flow-by condition at a flow rate of 500 mL/min.

After assembling, electrolyte was sufficiently purged into the AWE, with a continuous flow rate of 500 mL/min, to remove gas in the flow field and to wet the electrodes. A series of electrochemical characterizations of the four electrodes were further performed. As a first step, the electrochemical active surface areas (ECSAs) of the four electrodes were characterized by measuring their double-layer capacitances, and the values are given in **Figure 2A** (also see the experimental section for the detailed characterization method and procedure). Thanks to the porous structures of the four electrodes, their ECSAs were all greater than the projection area of 300 mm<sup>2</sup>. In comparison with their untextured counterparts, the ECSAs of the LNM and LNF were surprisingly enlarged by factors of 30% and 300%, respectively. Furthermore, the specific surface areas of the four electrodes, as the quotient of the ECSA and the corresponding volume, were also calculated (**Figure 2A**). It is noted that the two laser patterned electrodes possessed the highest specific surface areas above  $2.5 \times 10^4 \text{ m}^{-1}$ . This is one order of magnitude higher than a previously reported value of  $2.26 \times 10^3 \text{ m}^{-1}$  that was obtained from a wicking

NF with comparable geometrical factors but without laser textured patterns.<sup>47</sup> The high specific surface area of LNF not only indicates its good internal wetting but may also suggest that the laser textured patterns induced more reaction sites due to the higher local surface roughness. In comparisons, the hydrophobic NM present a specific surface area of  $2.08 \times 10^4 \text{ m}^{-1}$ , which was slightly lower but comparable to the values of the two laser patterned electrodes. This is because the thin mesh structure was in direct contact with the bulk electrolyte in the AWE, and a proper wetting was easy to achieve. In contrast, the specific surface area of the hydrophobic NF was about only 1/4 of the values of the other three electrodes. This implies that its permeability to the liquid electrolyte may be significantly lower than that of the LNF, due to the additional capillary pressure required for the electrolyte to enter the pores of NF.

To demonstrate the HER performance of the four electrodes, galvanostatic electrolysis measurements at different flow conditions were conducted. These experiments were repeated multiple times for ensuring the reproducibility. **Figure 2B & C** plot the recorded potential curves of these electrodes operated at a constant current density of  $80 \text{ mA/cm}^2$  (normalized to their projection area of  $300 \text{ mm}^2$ ), with and without applying a flow-by condition at a flow rate of  $500 \text{ mL/min}$ , respectively. As a matter of fact, without applying the flow-by condition, the produced bubbles trended to accumulate in the closed AWE environment, which gradually increased the cell ohmic resistance. As a result, all the four electrodes required increasingly greater voltages for maintaining the electrolysis at a constant current, as shown in **Figure 2B**. Moreover, with applying the flow-by condition, the different transport properties of the four electrodes are more clearly presented. Specifically, **Figure 2C** clearly reveals the performance improvements of LNM and LNF featured by their stabilized voltages at relatively low levels, comparing with the values of their nonpatterned counterparts. While, at a same operating condition, the voltages of the NM and NF gradually increased with irregular fluctuations. It is also noted that, at this operating condition, the voltage of LNM was approx.  $40 \text{ mV}$  lower than that of the LNF, which may infer the best bubble removal performance of the LNM among the four investigated electrodes. In contrast, the NM required the highest voltages at the both operating conditions.

In order to elucidate the mechanisms of such electrode wettability and structure modulated HER performance, we further performed volumetric SAM imaging for quantitatively analysing the two-phase transport behaviours in the four electrodes.

## 2.2 Operando volumetric SAM imaging

**Figure 3 A** illustrates the volumetric SAM image acquisition scheme, in which the entire cathode flow field of the AWE was designated as the region of interest (ROI). In the experiments, we used a  $75 \text{ MHz}$  transducer (i.e., capable of generating  $13 \text{ ns}$  pulses) equipped with a spherical acoustic lens with a diameter of  $6 \text{ mm}$  and a focal length of  $20 \text{ mm}$ . The beam profile of this transducer in our AWE environment is depicted by **Figure 3B**, and theoretically modelled in **Note S1**. Thus, scanning the focal zone over the ROI, we were able to realize the highest spatial resolution provided by the transducer,<sup>48</sup> namely a lateral resolution of  $70 \mu\text{m}$  (on the XY plane) and an axial resolution of approx.  $10 \mu\text{m}$  corresponding to the half spatial length of the pulse (along the Z direction) within a depth of focus (DOF) of approx.  $1.6 \text{ mm}$ . For SAM imaging, the height of the transducer (the Z position) was properly adjusted before image acquisition to ensure that the ultrasonic waves were properly focused in an electrode, as shown in the zoom-in view of **Figure 3A**. Since the DOF of the selected transducer perfectly overlaid the thicknesses of the investigated electrodes, we were able to acquire volumetric images of the two-phase transport inside the porous electrodes without further adjusting the height of transducer. In other words, the transducer was only scanned point-by-point over the horizontal plane above the ROI with high precision of  $0.1 \mu\text{m}$ , at the constant height. Considering the lateral resolution of  $70 \mu\text{m}$  enabled by the transducer, a scanning step size of  $20 \mu\text{m}$  was set for balancing the imaging quality and image update rate i.e., the voxel sizes in the X and Y directions were both  $20 \mu\text{m}$ . The scanning procedure took  $180 \text{ s}$

to acquire all A-scan signals for constructing each volumetric frame within an area of  $900 \text{ mm}^2$  ( $30 \text{ mm} \times 30 \text{ mm}$ ).

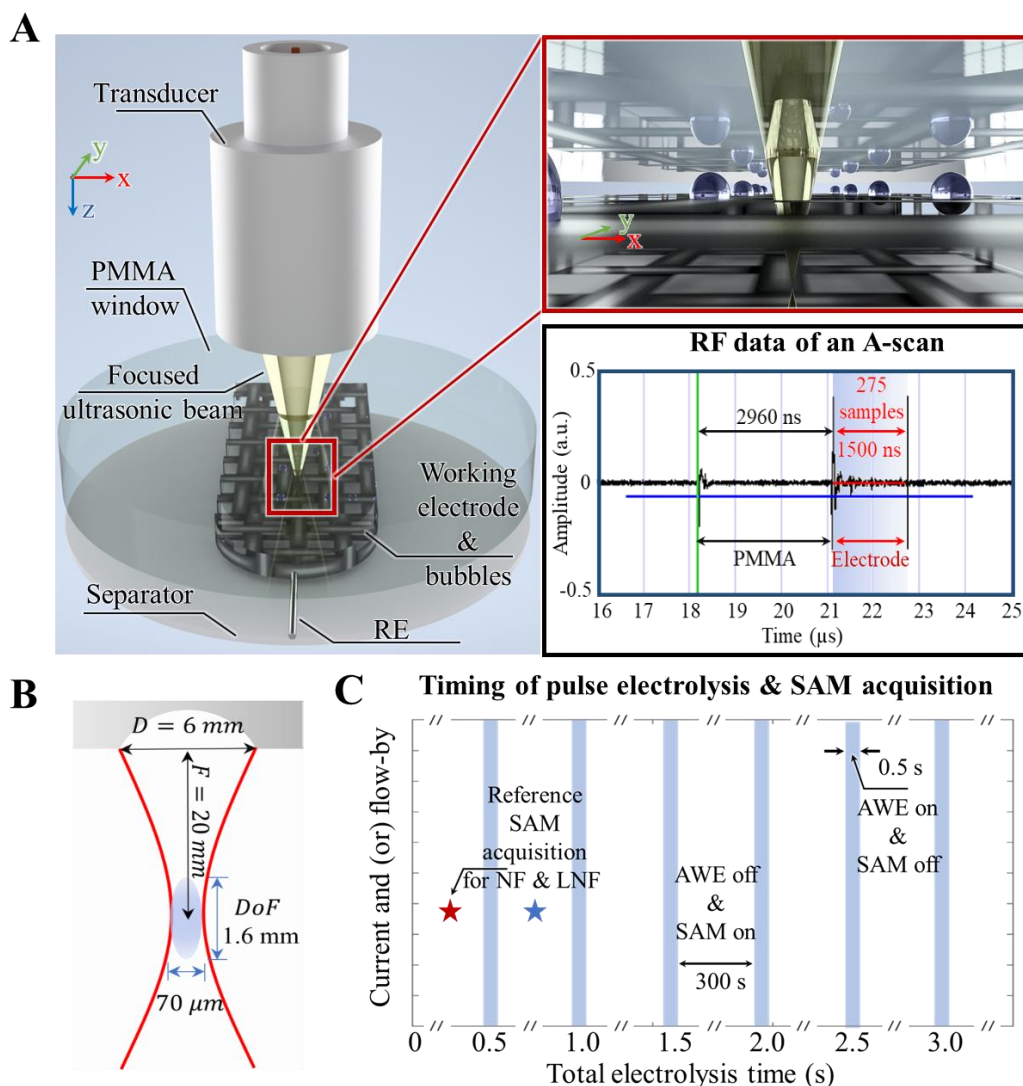


**Figure 3. The schematic representation of the volumetric SAM image acquisitions of the *operando* AWE.**

(A) The volumetric SAM imaging scheme, in which the red box shows a local zoom-in view indicating that the ultrasonic waves are focused inside of the electrode by properly adjusting the transducer's height. The black box plots an A-scan signal acquired from the NF, and the time window marked by the blue shade was reconstructed to the volumetric images.

(B) The ultrasound beam profile of the selected 75 MHz transducer, in which  $D$  and  $F$  are the diameter and focal length of the acoustic lens, respectively.

(C) The pulse electrolysis scheme for mimicking time resolved visualization of the mass transport in electrodes.

Moreover, at each scanning position, a short ultrasound pulse was excited and the echo signal due to the huge acoustic impedance mismatches among produced gas bubbles, the liquid electrolyte and the metallic electrodes was recorded, which is known as the A-scan. For instance, the black box of **Figure 3A** plots an A-scan signal acquired from the NF, and the electrode position is identified as the time window marked by the blue shade, in which the echo wave packets representing the phase interfaces at different depths were received at the corresponding transient times. Finally, all the acquired A-scan signals were constructed to the volumetric images, by converting the power of each sampling point in this designated time window to the greyscale value of a voxel at the corresponding registered position (see the experimental section for more details). Taking a homogenous speed of sound in the electrolyte

of 1580 m/s (see **Table S1** for the materials' acoustic properties), the selected time window lasting 1500 ns with 275 sampling points resulted to an equivalent penetration depth of 1.185 mm ( $1580 \text{ m/s} \times 1500 \text{ ns} / 2 = 1.185 \text{ mm}$ ) and a voxel size of approx.  $4.3 \mu\text{m}$  ( $1.185 \text{ mm} / 275 \approx 4.3 \mu\text{m}$ ) in the Z direction. The resulted penetration depth was sufficient for studying bubble dynamics of the thin NM and LNM, but it was not able to cover the entire thickness of the NF and LNF. This was limited by the low SNR at deeper positions in the complex open cell foam structures, because of strong scattering caused acoustic attenuation. It is however noticed that the penetration depth was mainly limited by our technical implementation, as a first proof-of-concept using this approach, rather than the SAM imaging technique itself. Higher SNR can be achieved by using either ultrasonic transducers with larger element sizes or focal lens with larger numerical apertures.

Nevertheless, it is important to justify the temporal resolution of SAM towards real-time imaging. S. De Angelis *et al.* previously reported an image update rate of 1.4 s per volumetric frame of bubble transport in PEMWE within a much smaller ROI of  $3.3 \text{ mm} \times 4.6 \text{ mm}$ , which was realized by one of the most cutting-edge synchrotron X-CT system.<sup>35</sup> Normalized to a same ROI dimension, with the current scanning speed, our SAM imaging system is able to realize a comparable speed of 3 s per volumetric frame. Moreover, thanks to the pointwise scanning nature of SAM, we are able to realize higher temporal resolution beyond sub-second by e.g., simultaneous scanning of multiple ultrasonic transducers or using customized transducer arrays.<sup>49</sup> Given the relatively slow image acquisition speed, limited by the huge ROI dimension of our test AWE, we introduced a pulse electrolysis scheme for mimicking the visualizations of time resolved two-phase transport in the electrodes, as shown in **Figure 3C**. Briefly, in each on-period of 0.5 s, a constant electrical current and the electrolyte flow with a flow rate of 500 mL/min were simultaneously applied (if the flow-by condition was applicable). Such a flow rate was sufficient for displacing the electrolyte in the entire cathode flow field with a volume of approx. 1 mL in 0.5 s. Therefore, in terms of bubble removal, the duration of the on-period was eligible to mimic the electrolysis under continuous flow-by. Each on-period was followed by a zero-current (and zero flow rate) off-period of 300 s, which allows for recording and storing the volumetric images of the two-phase transport in the previous on-period (see the experimental section for more details). Moreover, the bubbles produced in a previous on-period remained static during the following off-period for image acquisition, i.e., they neither move or dissolve (refer to **Figure S3 & S4** for the stability of the produced bubbles). The pulse electrolysis scheme addressed six electrolysis steps corresponding to a total electrolysis time of 3 s. Furthermore, in total seven volumetric frames were acquired for each electrode investigated at a specific operating condition, including the initial state after cell conditioning before electrolysis and the state after each 0.5 s electrolysis step.

### 2.3 Performance evaluations of SAM imaging and quantification of gas contents

To demonstrate the SAM imaging capability, **Figure 4A** shows an overview image of the LNM in the AWE before electrolysis rendered in greyscale, where the 3D printed flow field, the Pt wire RE, the periodical mesh grids, the separator beneath, and the gas bubbles are clearly visible. Moreover, **Figure 4A** depicts that the gas bubbles on the surfaces of the mesh electrodes were featured by their higher echo intensities represented by the darker greyscale colours, due to total acoustic reflections at the electrolyte-gas interfaces (see **Table S1**). Thus, for quantifying the gas contents of the two mesh electrodes, a greyscale thresholding was introduced for isolating the resolved bubbles (see experimental section for details). For example, the gas bubbles attached to the LNM in **Figure 4A** is segmented and the XY projection is shown as a binary image in the blue box, in which the clusters of tiny bubble (black circles) on the mesh wire, the smaller bubbles at the kink point of two wires (red circles) and larger bubbles confined in the pore (green circles) are clearly observed.

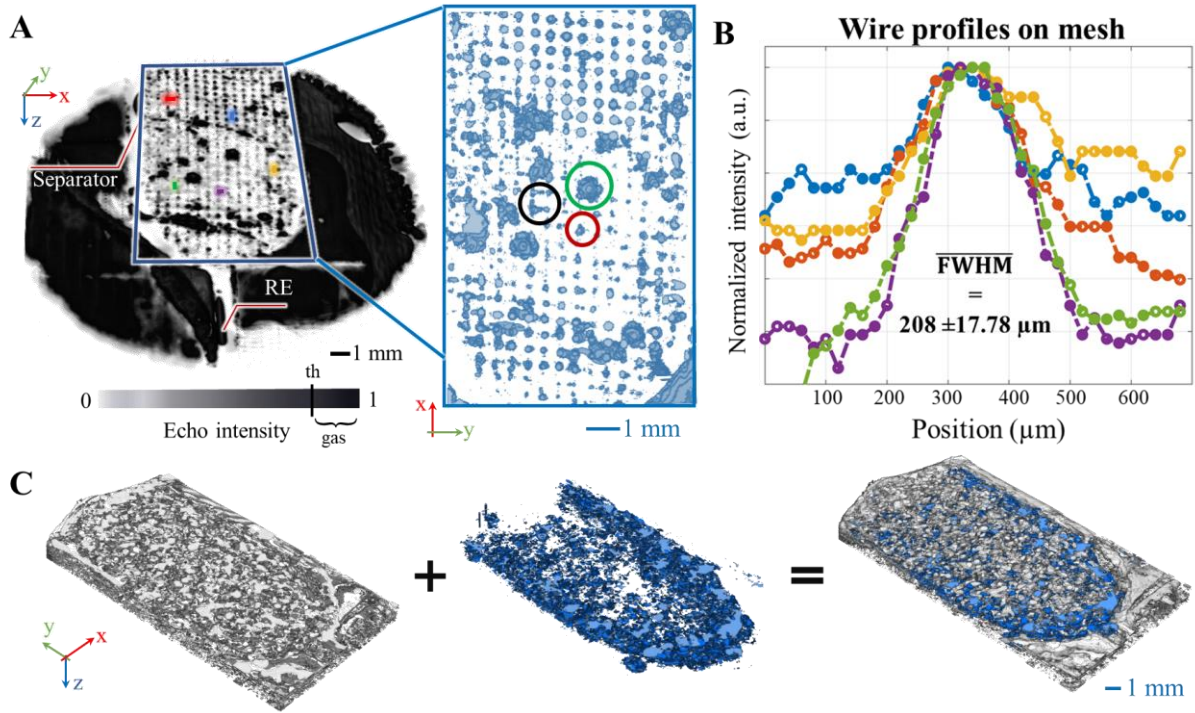


**Figure 4. Performance evaluations of SAM imaging and quantification of gas contents.**

(A) 3D volume rendering of the LNM in the AWE before electrolysis, in which the greyscale colormap indicates the echo intensity. The threshold value for isolating the bubbles is depicted. The binary image of bubbles attached to the LNM after segmentation is displayed in the blue box.

(B) The wire profiles at the five positions marked by the short dash lines in **Figure 4A** for evaluating the actual resolution and detectability, in which the mean value and standard deviation of the five profiles is given.

(C) A graphical visualization of isolating the produced bubbles from the open cell foam electrodes: the NF in the AWE before electrolysis is firstly resolved as a reference (left); the spatial distribution of  $H_2$  bubbles produced in the following electrolysis step i.e., the blue star in **Figure 3C** is determined from the difference image of the two volumetric frames; the right image thus renders the  $H_2$  bubbles in the pore networks of the NF.

It is also important to evaluate the actual spatial resolution and detectability, where the well-defined dimensions of the mesh grid provided a great opportunity. **Figure 4B** plots the wire profiles at multiple different positions on the grid marked by the short dash lines in **Figure 4A**, in which the mean value and the standard deviation of these profiles in the SAM images i.e., the full width half maximum (FWHM) of these profiles was determined as  $208 \pm 17.78 \mu\text{m}$ . This is in average approx.  $68 \mu\text{m}$  thicker than the actual wire diameter of  $140 \mu\text{m}$ , which implies that the realized lateral resolution was in a good agreement with the theoretical value of  $70 \mu\text{m}$ . This allowed us to resolve two bubbles with a distance farther than  $70 \mu\text{m}$  and single bubbles with a diameter bigger than this value from the SAM images. Thanks to high resolution imaging, the total volume of gas bubbles attached to the mesh electrodes and their coverages were able to be quantified. Specifically, the gas volume was obtained by counting the total number of voxels designated as gas in the binary volumetric images after segmentation, as given in **Equation 1**, in which  $vol_{vox} = 20 \times 20 \times 4.3 \mu\text{m}^3$  stand for the volume of a voxel.

$$V_{gas} = vol_{vox} \cdot \sum n|_{vox=Gas} \quad (\text{Equation 1})$$

While, given the 2D nature of the woven mesh electrodes, their coverages were evaluated only on the XY projection, as given in **Equation 2**, in which  $A_{px} = 20 \times 20 \mu\text{m}^2$  and  $S$  stand for the pixel size and the total projection area under evaluation, respectively. These two quantities directly lead to the ohmic loss ( $\eta_{bub\_ohm} \propto |j| \cdot V_{gas}$ ) due to the electrical resistances of gas bubbles, and the bubble coverage

overpotential ( $\eta_{bub} \propto \theta$ ) that is resulted from the elevated local current densities at the rest of the uncovered reaction sites, respectively.<sup>47</sup>

$$\theta = A_{px} \cdot \sum n|_{px=Gas}/S \quad (\text{Equation 2})$$

Unlike the distinct echo intensities of gas bubbles and the mesh electrodes, the bubbles in the open cell foam did not necessarily exhibit greater echo intensities than the electrodes, especially at deeper positions. This is because of the complicated and unpredictable diffractive scattering of ultrasonic waves in such irregular porous medium (see **Figure S2** for more detailed illustrations). This hindered us to directly segment the gas contents from the NF and LNF using the aforementioned greyscale thresholding method. Instead, considering an open cell foam electrode as a static and time-invariant background, it is more accurate to determine the variation of gas contents after each pulse electrolysis step against the initial value before electrolysis. In this work, this was done by subtracting the volumetric frame acquired at the initial state as reference and the other one acquired after an on-period (see the experimental section for more detailed digital image processing). For instance, **Figure 4C** displays the volumetric images of the NF before and after the first electrolysis step (indicated by the red and blue stars in **Figure 3C**) without the flow-by condition, in which the initial state of NF and the generated bubbles are shown as grey and blue, respectively. The electrode coverage and gas volume in such complex 3D structures can both be well represented by the volume fraction of pores occupied by the bubbles, as given in **Equation 3**, in which volumes of pores and produced bubbles were determined from the initial image and difference images, respectively.

$$VF = V_{gas}/V_{pore} = \sum n|_{vox=Gas}^{difference} / \sum n|_{vox=Pore}^{initial} \quad (\text{Equation 3})$$

Although SAM was not able to directly visualize the electrolyte that served as homogeneous medium for ultrasound propagation i.e., no reflection, we show later that the electrolyte transport can be deduced from the resolved bubble behaviours.

## 2.4 Impacts of surface wettability on the HER performance of woven mesh electrodes

We now discuss the surface wettability modulated two-phase transport and the resulted HER performance of the NM and LNM based on the quantitative SAM visualizations. **Figure 5A & B** plot the total volumes of gas bubbles attached to the NM and LNM and their coverages over time at the different operation conditions, respectively. The quantified gas contents of the two mesh electrodes were in similar trends with the above discussed their voltages during galvanostatic electrolysis. We started from a geometrical current density of 40 mA/cm<sup>2</sup> and without the flow-by condition, in which the coverages of the two electrodes both increased 14 %, throughout the electrolysis process of in total 3 s. The total volumes of gas bubbles attached to the two electrodes also increased a comparable amount i.e., 0.626  $\mu$ L for LNM and 0.702  $\mu$ L for NM (see **Figure S3 & S4** for the time lapse images of bubble accumulations on the two electrodes' surfaces). However, the residual air content of NM after cell conditioning and before electrolysis was almost twice of that of LNM. **Figure 5C** displays these residual air bubbles attached to the NM, which masked a certain fraction of the reaction sites and therefore well explains the lower ECSA of NM. Moreover, after the electrolysis of 3 s, the total gas content on NM was nearly same as that of the LNM operated at a higher current density of 80 mA/cm<sup>2</sup> without flow-by condition where bubbles evolved more rapidly (compare **Figure 5D & F**). The quantitative SAM visualizations thus provide us important insights to better interpret the higher voltage of NM operated at larger current densities. The high coverage of NM due to residual air trapping, on one hand, effectively increased the local current densities on the remaining active electrode surface i.e., the current density normalized to the ECSA ( $j_{ECSA}$ ), which resulted to higher activation overpotentials ( $\eta_{act} \propto j_{ECSA}$ ) to

trigger the HER.<sup>50</sup> Moreover, at higher current densities, the ohmic losses due to electrical resistance of these bubbles with large volume were also amplified.

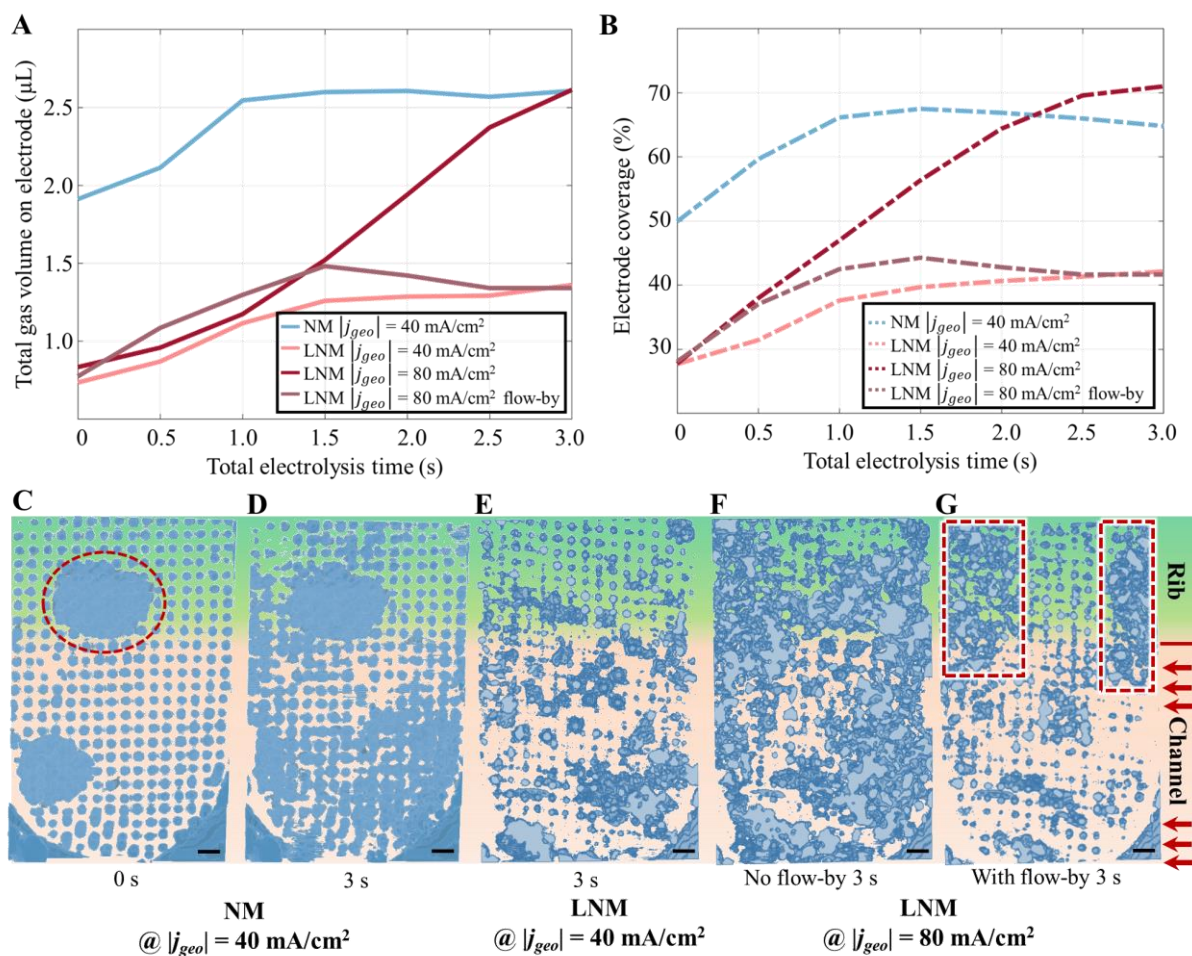


**Figure 5. Quantitative SAM visualizations of the gas bubbles on the NM and LNM.**

(A) The total volumes of gas bubbles attached to the NM and LNM over time at the different AWE operating conditions.

(B) The coverages of NM and LNM over time at different AWE operating conditions.

(C) – (G) The XY projections indicating the spatial distributions of gas bubbles attached to the woven mesh electrodes at the different operating conditions and electrolysis time. The positions of the straight flow channel and the rib are marked by different colours, respectively. The arrows indicate the direction of the applied flow-by condition. Scale bar is 1 mm.

(C) The residual bubbles attached to the NM at the initial state i.e., after cell conditioning and before electrolysis. The red circle indicates the big bubble under rib that was not able to be removed during the continuous electrolyte purging.

(D) The gas bubbles attached to the NM after a total electrolysis time of 3 s, at a geometrical current density of 40 mA/cm<sup>2</sup> without the flow-by condition.

(E) The gas bubbles attached to the LNM after a total electrolysis time of 3 s, at a geometrical current density of 40 mA/cm<sup>2</sup> without flow-by condition.

(F) The gas bubbles attached to the LNM after a total electrolysis time of 3 s, at a geometrical current density of 80 mA/cm<sup>2</sup> without the flow-by condition.

(G) The gas bubbles attached to the LNM after a total electrolysis time of 3 s, at a geometrical current density of 80 mA/cm<sup>2</sup> with the flow-by condition. The red rectangles indicate the slight bubble retentions that was not removed by the flow-by.

Furthermore, we elucidate the mechanism of gas entrapments of the NM. **Figure 5C** shows that, after cell assembling and continuous electrolyte purging, all the pores of the NM trapped air bubbles, and

they were formed by the so-called bypass trapping mechanism.<sup>51</sup> More precisely, the electrolyte, being the non-wetting phase for the hydrophobic NM, preferred to flow on the surfaces of the NM as low resistance pathways, rather than invading the pores and displacing the gas phase inside. This is because the latter requires an additional force to be applied vertically to the electrolyte-gas interface i.e., perpendicular to the electrode surface for overcoming the capillary pressure. However, the flow-by condition in our experiments provided mostly horizontal force to the electrolyte in parallel to the surface of NM. In contrast, the wicking state of the LNM reduced the resistance of electrolyte flowing into its pores i.e., lowered the capillary pressure. As a result, only a few residual air bubbles were found on the LNM before electrolysis, as already being shown in **Figure 4A**.

Nevertheless, bubbles on the hydrophobic NM were subjected to higher surface tension forces against the shear forces provided by the flow-by condition. In other words, their removal required higher flow rates, comparing with the bubbles on the wicking LNM. The inferior bubble removal performance of NM is directly represented by the bigger millimeter-sized bubble that initially adhered to the NM (red circle in **Figure 5C**). We were not able to remove it by the continuous electrolyte purging at a flow rate of 500 mL/min, which however did not take place on the LNM (**Figure 4A**). In contrast, the resolved gas contents on the LNM, at the current density of 80 mA/cm<sup>2</sup> and different flow conditions, more clearly revealed its superior bubble removal performance. **Figure 5A & B** show that, without applying the flow-by condition, the bubbles rapidly accumulated on the surface of LNM within a total electrolysis time of 3 s. **Figure 5F** displays these produced bubbles that occupied most of the LNM surface except the middle part, likely due to the lower local current density distributions (see also **Figure S5** for the time lapse), given the ring shape of the CE (see **Figure S1**). With the flow-by condition, the gas contents on the LNM showed a slight overshoot before 1.5 s and then stabilized at a low level that was almost half of the situation without flow-by applied. **Figure 5G** indicates that, in the flow channel, most of the produced bubbles on the LNM were removed by the flow, and only slight bubble retentions on the edge of LNM under the rib were observed (red dash rectangular), probably because of the internal convections in that area. All the images of bubbles on the NM and LNM at these operating conditions during the pulse electrolysis process are given in **Figure S3 – Figure S6**.

## 2.5 Impacts of surface wettability on the HER performance of open cell foam electrodes

As a next step, we discuss the quantitative SAM imaging revealed influences of the surface wettability of the open cell foam electrodes to their transport properties and therefore HER performance. Likewise, **Figure 6A** plots the volume fractions of gas in NF and LNF at the different flow conditions at the current density of 80 mA/cm<sup>2</sup>. Without flow-by, the bubbles accumulated both in NF and LNF with an overall similar trend, which is in good agreement with the variations of their voltages. Given the fact that the ECSA of NF was only 1/4 of that of the LNF, and considering its macroscopic hydrophilicity, the NF might trap a greater amount of air during the initial electrolyte purging for cell conditioning (similar as the NM did). However, limited by our current subtraction-based bubble segmentation scheme, we were not able to directly resolve the initial gas entrapments in NF and LNF. Instead, we derived their internal wetting states from the nucleation sites of H<sub>2</sub> bubbles and their evolution pathways of in the two electrodes. More precisely, **Figure 6B & C** show the spatial distributions of H<sub>2</sub> bubbles generated in LNF and NF after electrolysis and without applying the flow-by condition. We clearly observed large and continuous H<sub>2</sub> clusters accumulating on the edge of LNF. On the contrary, the H<sub>2</sub> bubbles in the NF was more distributed and in form of small clusters (see also **Figure S7 & S9** for time lapse images). It is hypothesized that the initial air trapping in some pores of NF deactivated part of the reaction sites, and therefore separated the nucleation spots and evolution pathways of the H<sub>2</sub> bubbles.

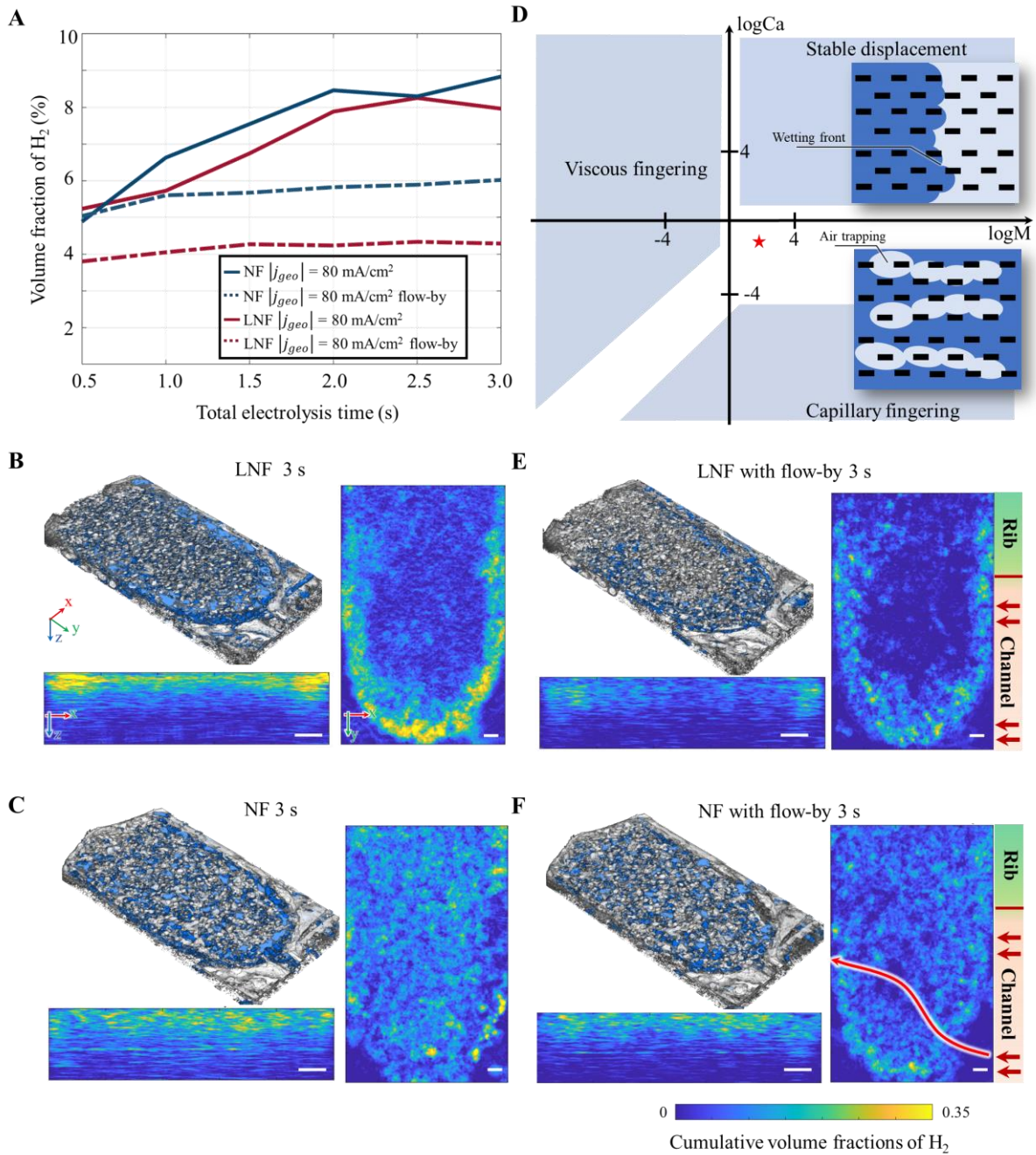


**Figure 6. Quantitate SAM visualizations of the gas bubbles in the NF and LNF.**

(A) The volume fractions of produced bubbles in NF and LNF at the current density of  $80 \text{ mA/cm}^2$  and different flow conditions.

(B) – (C) The spatial distributions of produced  $H_2$  bubbles in the LNF (B) and NF (C) after a total electrolysis time of 3 s at a current density of  $80 \text{ mA/cm}^2$  and without the flow-by condition. The grey and blue stand for the electrode and  $H_2$  bubbles, respectively. The 2D images show the cumulative volume fractions of  $H_2$  in the porous electrodes along the XY and XZ projections, in which the positions of the flow channel and rib are indicated as well. The red arrows show the flow-by direction. Scale bar is 1 mm.

(D) The general phase diagram of the different flow regimes for the drainage process adapted from,<sup>52</sup> in which the red star corresponds to the condition of displacing air in the NF in our experiments.

(E) – (F) The spatial distribution of produced  $H_2$  bubbles in the LNF (E) and NF (F) after a total electrolysis time of 3 s at a current density of  $80 \text{ mA/cm}^2$  and with the flow-by condition. Scale bar is 1 mm. The red arrows in (E) and (F) show the flow-by direction and the low-resistance electrolyte pathway in NF, respectively.

We further validated our observations and analysis by the theory of immiscible two-phase flows in porous media. We considered the logarithm viscosity ratio ( $\log M$ ) of the electrolyte as the invading phase and air as the defending phase in NF, as well as the logarithm capillary number ( $\log Ca$ ) of supplying electrolyte to AWE flow field with a flow rate of 500 mL/min. Taking the material properties at the room temperature (25 °C) from,<sup>53–55</sup> the value of  $\log M$  was as 1.68, as calculated in **Equation 4** where  $\mu$  stands for the dynamic viscosity of fluid.

$$\log M = \log \left( \frac{\mu_{KOH_{8wt\%}}}{\mu_{H_2}} \right) = \log \left( \frac{0.89 \times 10^{-3}}{1.85 \times 10^{-5}} \right) \approx 1.68 \quad (\text{Equation 4})$$

The  $\log Ca$  was estimated to be -1.29, as given in **Equation 5**, in which  $v$  stands for the flow velocity that was approx. 4 m/s corresponding to the flow rate and the geometry of the flow channel, and  $\sigma$  is the surface tension of the electrolyte.

$$\log Ca = \log \left( v \cdot \frac{\mu_{KOH_{8wt\%}}}{\sigma} \right) = \left( 4 \cdot \frac{0.89 \times 10^{-3}}{70 \times 10^{-3}} \right) \approx -1.29 \quad (\text{Equation 5})$$

Given the fact that the electrolyte was the non-wetting phase of NF, the values of  $\log M$  and  $\log Ca$  suggest that the flow regime of replacing air with the electrolyte in NF was at the transition region between the capillary fingering and stable displacement.<sup>52</sup> **Figure 6D** shows the general phase diagram of the different flow regimes for the non-wetting phase displacing the wetting phase in porous medium that is termed as “drainage”.<sup>52</sup> The red star in **Figure 6D** indicates the flow regime of the supplying electrolyte to NF in our experiments, which was located in the transition region between the capillary fingering and the stable displacement. Following the schematic diagrams of the two-phase flow patterns in the pore network, in such a transition region, the electrolyte might unable to completely replace all the air in the NF pore network, especially smaller ones due to higher capillary pressure required, which caused gas trapping to a certain extent. This unavoidably led to higher overpotentials of the NF. On the contrary, the electrolyte served as the wetting phase for the wicking LNF, and the process of displacing air (as non-wetting phase) with electrolyte in the LNF is referred as “imbibition” among literatures.<sup>56,57</sup> Based on the phase diagrams of flow regimes of imbibition process in,<sup>56</sup> with the same capillary number of  $\log Ca \approx -1.29$ , the electrolyte was able to realize piston-like frontal advances in the wicking LNF, resulting to a negligible gas entrapment (the flow pattern of the piston-like frontal advance is visually the same as stable displacement in **Figure 6D** but follows a different mechanism).

The different flow patterns of the electrolyte in the NF and LNF, influenced by their surface wettability, also affected their bubble removal performance under the flow-by condition. **Figure 6A** shows that, with applying the flow-by, the volume fraction of  $H_2$  bubbles in LNF was stabilized at around 4%, while the value of NF gradually increased from 5% to 6% throughout the in total 3 s electrolysis process. These values were in line with the aforementioned lower overpotential on the LNF. The spatial distributions of  $H_2$  bubbles in LNF and NF after electrolysis under the flow-by condition are shown in **Figure 6E & F**, respectively. Apparently, the piston-like frontal advances of electrolyte in the LNF resulted to its superior bubble removal performance. We clearly see that the continuous bubble clusters accumulated on the edge and smaller bubbles in the middle part of LNF were removed by the flow. While, a few separated residual bubbles were found mainly on the edge of LNF, considering the higher local pressure due to rapid evolution of  $H_2$  bubbles as a counter force against the electrolyte flow for removing them. In contrast, the non-perfect stable displacement of electrolyte in NF made the produced bubbles more difficult to be completely removed under the flow-by condition. This resulted to a high residual  $H_2$  volume fraction in the NF and therefore its higher overpotentials, as shown in **Figure 6F**. Nevertheless, the spatial distributions of the residual  $H_2$  bubbles rendered a low resistance pathway of

the electrolyte flow (see the red arrow), mainly through the middle of the NF, where the bubble evolution rate was slower (also see **Figure S8** for time lapse images). The images of bubbles in the NF and LNF at all the operating conditions during the pulse electrolysis process are given in **Figure S7 – Figure S10**.

## 2.6 Summary

In summary, the quantitative SAM visualizations revealed the underlying mechanisms of the decreased overpotentials of wicking electrodes, namely less trapping of residual air contents that reduces their activation overpotentials, and better bubble removal performance for decreasing their transport overpotentials i.e.,  $\eta_{bub}$  and  $\eta_{bub\_ohm}$ . The wicking LNM and LNF investigated in our experiments are therefore promising for the purpose of AWEs with improved performance. Moreover, in comparison with the LNF, the LNM present superior bubble removal performance, and therefore a lower voltage required for HER in our experimental environment and conditions. This was because the electrolyte flowing on the surface of LNM was subjected to lower resistance than in the complicated and tortuous pore networks of the LNF. Thus, our SAM visualization results provided constructive insights towards future optimizations. Firstly, aiming for a minimized transport overpotential, the hydrophilicity of the current LNM and LNF should still be enhanced i.e., to lower their contact angles for reducing the surface tension force of bubbles and facilitating their removal. Taking the advantage of our laser texturing technique, this can be realized by adjusting the depth and distance of the groove structures. Alternatively, for the given wettability of the current LNM and LNF, more efficient water splitting could be achieved by electrodes with optimal pore size and pore network structure that can simultaneously enable large ECSA and superior bubble removal. Nevertheless, appropriate flow field designs based on the resolved two-phase transport behaviours in a specific electrode are in general beneficial for reducing the cell voltage required in practical applications. Following these guidelines, in further researches, we will iteratively optimize these AWE related designs and thoroughly investigate their performance in industry or technical relevant environments and conditions.

## 3. CONCLUSIONS AND OUTLOOKS

In this work, we experimentally demonstrated the use of high-resolution volumetric SAM imaging technique for quantifying two-phase transport behaviours in porous Ni electrodes of *operando* AWEs. Such an affordable, accessible and high-performance ultrasonic imaging technique allowed us to study the underlying mechanisms of overpotentials modulated by the structures and wettability of electrodes, close to their practical operating environment and conditions. Taking the advantages of SAM instrumentation, we obtained these important design guidelines towards high efficiency AWEs on a regular laboratory base, which would otherwise require expensive and complicated X-ray and neutron CT systems. Given the fact that electrochemically gas-evolving systems present in a wide range of industrial energy conversion and storage applications, this work not only contribute to AWE related developments but also pioneers the use of SAM instrumentations for expanding our understandings on general two-phase transport related limitations for such electrochemical systems. Encouraged by such an ambitious purpose, in future works, we dedicate to refine the current SAM instrumentation and image processing approaches in order to develop a fully automated working pipeline for long-term and real-time imaging of dynamic two-phase transport in such gas-evolving electrochemical systems.

## EXPERIMENTAL PROCEDURES

### Electrodes preparations

The Ni woven mesh sheets and open cell foam used in this work were obtained from HAVER & BOECKER and Fraunhofer IFAM Dresden, respectively.

The laser texturing process was carried out using a picosecond slab-shaped solid-state laser (Edgewave InnoSlab, Würselen, Germany) emitting at a wavelength  $\lambda$  of 532 nm and with a pulse width of 12 ps. The laser beam is guided by high reflective mirrors towards a beam expander and further to a 2D-galvo scanner (Raylase Super Scan III, Weßling, Germany). Furthermore, a f-theta lens is applied with a focal length of 100 mm, leading to a beam diameter in the focal plane of 18  $\mu\text{m}$ . The scanning velocity was set to 6.25 mm/s with a pulse repetition of 10 kHz and a pulse energy of 100  $\mu\text{J}$ . The texturing process was performed using a unidirectional scan strategy. Cross-like and line-like patterns were generated on the LNM and LNF, respectively. The spacing between of each generated structure was set to 40  $\mu\text{m}$  for all investigated specimen.

### Electrode contact angle characterization

The apparent contact angles of the two hydrophobic i.e. unstructured electrodes were measured by the sessile droplet method by applying droplets of 8 wt% KOH solution on the surfaces of the electrodes. While the Wilhelmy plate method was applied to measure the other two hydrophilic i.e. laser structured electrodes,<sup>58</sup> in which the electrodes were immersed into the KOH solution. Multiple images of each electrode were captured by a digital camera (Pentax K1) equipped with a macro lens. The contact angles were then obtained in ImageJ.<sup>59</sup>

### Surface morphology characterization of open cell foam electrodes

The surface morphologies of the four electrodes were acquired using a scanning electron microscopy (Zeiss 1540 XB) with a 20 kV accelerating voltage.

### Electrochemical characterizations of the electrodes

The electrochemical characterizations and galvanostatic electrolysis were performed with an electrochemical workstation (CHI660I, Corrtest Instruments, USA). The ECSAs of the four electrodes were determined by comparing their double layer capacitances ( $C_{dl}^{WE}$ ) with a unit value of 35  $\mu\text{F}/\text{cm}^2$  obtained from a flat Ni foil ( $C_{dl}^{flatNi}$ ) with well-defined surface area, as given in **Equation 6**.<sup>19,20</sup> Moreover, the double layer capacitance values of the electrodes ( $C_{dl}^{WE}$ ) were obtained by cyclic voltammetry performed at different voltage scan rates ( $v$ ) around their open circuit potentials, and  $i_c$  in **Equation 6** is the measured capacitive current.

$$ECSA = \frac{C_{dl}^{WE}}{C_{dl}^{flatNi}} = \frac{v \cdot i_c}{35 \mu\text{F}/\text{cm}^2} \quad (\text{Equation 6})$$

### AWE operations

The home-made AWE was operated at room temperature, under atmospheric pressure, and supplied with 8 wt% KOH solution as electrolyte to ensure the chemical integrity of the 3D printed parts during experiments. A hose pump (MASTERFLEX L/S, Cole-Parmer, Germany) was connected to the AWE to supply electrolyte and adjust the flow rate. To avoid electrolyte leakage, the whole setup was firstly tested for tightness. Before experiments, electrolyte was sufficiently purged into the AWE to remove the gas trapped in the porous electrodes and adhered to their surfaces to the maximum extent.

It is noted that, given the low concentration of the KOH solution, we used the dynamic viscosity and surface tension values of water in **Equation 4 & 5**.

### **Volumetric SAM imaging process**

To ensure a good acoustic coupling, the AWE was immersed in an aquarium filled with Milli-Q water for SAM imaging. Given the huge electrical resistivity of Milli-Q water, the electrolysis was not affected by the water immersion. Volumetric SAM images were acquired using a commercial SAM system, capable of providing a scanning precision of 100 nm (SAM 501 HD<sup>2</sup>, PVA TePla AG, Westhausen, Germany). A more detailed overview of the system can be found elsewhere.<sup>60</sup>

Since the SAM control interface was not synchronized with the electrochemical workstation for the pulse electrolysis, each volumetric image was manually acquired and stored after each electrolysis step. This led to a longer off-period of 300 s for manual operations, although the scanning time for each volumetric frame took only 180 s.

The part of A-scan signal in between 18.20  $\mu$ s and 21.16  $\mu$ s plotted in the black box of **Figure 2A** corresponds to the round-trip ultrasound propagation time in the 4 mm PMMA plate ( $2700 \text{ m/s} \times 2.96 \mu\text{s} / 2 = 4 \text{ mm}$ ). Thus, the waveform after 21.16  $\mu$ s i.e., the rare surface of PMMA thus corresponds to the depths of the electrodes.

### **Post processing of volumetric SAM images**

The acquired volumetric SAM images were stored in format of multipage TIFF, and each page corresponds to an XY plane at a certain depth. These images were processed in MATLAB R2023a for localizing and quantifying the H<sub>2</sub> saturation in the electrodes. Specifically, each acquired volumetric image was firstly median filtered to remove any salt and pepper noise. For isolating gas contents from the woven mesh electrodes, the Otsu's method was used to determine overall threshold values for binarizing all the volumetric SAM images acquired from the NM and LNM, respectively. While the acoustic attenuation in the open cell foam did not allow us to determine overall threshold values for isolating bubbles from the NF and LNF. Thus, each slice representing a 2D image of the XY plane at specific depth was binarized individually i.e., different threshold values were used for images at different depths. The resulted binary volumetric images were median filtered for smoothing. This processing scheme was performed for the volumetric images acquire of the NF and LNF at the initial states and the difference images presenting the H<sub>2</sub> saturation after each electrolysis step. However, with the subtraction scheme, it is not possible yet to differentiate the initial gas contents from the foam electrodes. Future works will implement advanced image background removal approaches to solve this issue e.g., singular value decomposition (SVD) that requires more volumetric frames to accurately compute each singular vector.<sup>61</sup>

### **SUPPLEMENTAL INFORMATION**

Document S1. Supplemental Experimental Procedures, Figures S1–S10, Notes S1, and Table S1.

### **ACKNOWLEDGMENTS**

The authors would like to thank R. Nauber and H. Emmerich for valuable discussions, and B. Birki for the assistance on SAM experiments. The authors specially thank T. Djuric-Rissner for coordinating the collaborations between TU Dresden and PVA TePla Analytical Systems GmbH. This project is supported with funds provided by the Deutsche Forschungsgemeinschaft (DFG) under grant 512483557 (BU2241/9-1), the Helmholtz Association Innovation pool project "Solar Hydrogen" and the Hydrogen Lab of the School of Engineering of TU Dresden.

## Reference

1. Hassan, Q., Algburi, S., Sameen, A.Z., Salman, H.M., and Jaszczur, M. (2024). Green hydrogen: A pathway to a sustainable energy future. *Int. J. Hydrogen Energy* 50, 310–333. 10.1016/j.ijhydene.2023.08.321.
2. Crews, M.A., and Shumake, B.G. (2017). Hydrogen production. In *Springer Handbooks* (Wiley-VCH Verlag), pp. 787–816. 10.1007/978-3-319-49347-3\_24.
3. Kumar, S.S., and Lim, H. (2023). Recent advances in hydrogen production through proton exchange membrane water electrolysis - a review. *Sustain. Energy Fuels* 7, 3560–3583. 10.1039/d3se00336a.
4. Emam, A.S., Hamdan, M.O., Abu-Nabah, B.A., and Elnajjar, E. (2024). A review on recent trends, challenges, and innovations in alkaline water electrolysis. *Int. J. Hydrogen Energy* 64, 599–625. 10.1016/j.ijhydene.2024.03.238.
5. Li, W., Tian, H., Ma, L., Wang, Y., Liu, X., and Gao, X. (2022). Low-temperature water electrolysis: fundamentals, progress, and new strategies. *Mater. Adv.* 3, 5598–5644. 10.1039/d2ma00185c.
6. He, Y., Cui, Y., Zhao, Z., Chen, Y., Shang, W., and Tan, P. (2023). Strategies for bubble removal in electrochemical systems. *Energy Rev.* 2, 100015. 10.1016/j.enrev.2023.100015.
7. Xu, Q., Zhang, L., Zhang, J., Wang, J., Hu, Y., Jiang, H., and Li, C. (2022). Anion Exchange Membrane Water Electrolyzer: Electrode Design, Lab-Scaled Testing System and Performance Evaluation. *EnergyChem* 4, 100087. 10.1016/j.enchem.2022.100087.
8. Yuan, S., Zhao, C., Cai, X., An, L., Shen, S., Yan, X., and Zhang, J. (2023). Bubble evolution and transport in PEM water electrolysis: Mechanism, impact, and management. *Prog. Energy Combust. Sci.* 96. 10.1016/j.pecs.2023.101075.
9. Yang, H., Driess, M., and Menezes, P.W. (2021). Self-Supported Electrocatalysts for Practical Water Electrolysis. *Adv. Energy Mater.* 11. 10.1002/aenm.202102074.
10. Yang, F., Kim, M.J., Brown, M., and Wiley, B.J. (2020). Alkaline Water Electrolysis at 25 A cm<sup>-2</sup> with a Microfibrillar Flow-through Electrode. *Adv. Energy Mater.* 10. 10.1002/aenm.202001174.
11. Yu, L., Zhu, Q., Song, S., McElhenny, B., Wang, D., Wu, C., Qin, Z., Bao, J., Yu, Y., Chen, S., et al. (2019). Non-noble metal-nitride based electrocatalysts for high-performance alkaline seawater electrolysis. *Nat. Commun.* 10, 1–10. 10.1038/s41467-019-13092-7.
12. Yan, X., Biemolt, J., Zhao, K., Zhao, Y., Cao, X., Yang, Y., Wu, X., Rothenberg, G., and Yan, N. (2021). A membrane-free flow electrolyzer operating at high current density using earth-abundant catalysts for water splitting. *Nat. Commun.* 12, 1–9. 10.1038/s41467-021-24284-5.
13. Esposito, D. V. (2017). Membraneless Electrolyzers for Low-Cost Hydrogen Production in a Renewable Energy Future. *Joule* 1, 651–658. 10.1016/j.joule.2017.07.003.
14. de Groot, M.T., Kraakman, J., and Garcia Barros, R.L. (2022). Optimal operating parameters for advanced alkaline water electrolysis. *Int. J. Hydrogen Energy* 47, 34773–34783. 10.1016/j.ijhydene.2022.08.075.
15. Brauns, J., and Turek, T. (2020). Alkaline water electrolysis powered by renewable energy: A review. *Processes* 8. 10.3390/pr8020248.
16. Zhao, P., Wang, J., Sun, L., Li, Y., Xia, H., and He, W. (2024). Optimal electrode configuration and system design of compactly-assembled industrial alkaline water electrolyzer. *Energy Convers. Manag.* 299, 117875. 10.1016/j.enconman.2023.117875.
17. Chen, Q., Niu, Z., Li, H., Jiao, K., and Wang, Y. (2021). Recent progress of gas diffusion layer in proton exchange membrane fuel cell: Two-phase flow and material properties. *Int. J. Hydrogen Energy* 46, 8640–8671. 10.1016/j.ijhydene.2020.12.076.

18. Liu, H., Tao, H.B., and Liu, B. (2022). Kinetic Insights of Proton Exchange Membrane Water Electrolyzer Obtained by Operando Characterization Methods. *J. Phys. Chem. Lett.* *13*, 6520–6531. 10.1021/acs.jpcclett.2c01341.
19. Rox, H., Bashkatov, A., Yang, X., Loos, S., Mutschke, G., Gerbeth, G., and Eckert, K. (2023). Bubble size distribution and electrode coverage at porous nickel electrodes in a novel 3-electrode flow-through cell. *Int. J. Hydrogen Energy* *48*, 2892–2905. 10.1016/j.ijhydene.2022.10.165.
20. Krause, L., Skibińska, K., Rox, H., Baumann, R., Marzec, M.M., Yang, X., Mutschke, G., Żabiński, P., Lasagni, A.F., and Eckert, K. (2023). Hydrogen Bubble Size Distribution on Nanostructured Ni Surfaces: Electrochemically Active Surface Area Versus Wettability. *ACS Appl. Mater. Interfaces* *15*, 18290–18299. 10.1021/acsami.2c22231.
21. Kim, B.K., Kim, M.J., and Kim, J.J. (2021). Impact of Surface Hydrophilicity on Electrochemical Water Splitting. *ACS Appl. Mater. Interfaces* *13*, 11940–11947. 10.1021/acsami.0c22409.
22. Ziesche, R.F., Hack, J., Rasha, L., Maier, M., Tan, C., Heenan, T.M.M., Markötter, H., Kardjilov, N., Manke, I., Kockelmann, W., et al. (2022). High-speed 4D neutron computed tomography for quantifying water dynamics in polymer electrolyte fuel cells. *Nat. Commun.* *13*, 1–11. 10.1038/s41467-022-29313-5.
23. Tengattini, A., Lenoir, N., Andò, E., Giroud, B., Atkins, D., Beaucour, J., and Viggiani, G. (2020). NeXT-Grenoble, the Neutron and X-ray tomograph in Grenoble. *Nucl. Instruments Methods Phys. Res. Sect. A Accel. Spectrometers, Detect. Assoc. Equip.* *968*, 163939. 10.1016/j.nima.2020.163939.
24. Zlobinski, M., Schuler, T., Büchi, F.N., Schmidt, T.J., and Boillat, P. (2020). Transient and Steady State Two-Phase Flow in Anodic Porous Transport Layer of Proton Exchange Membrane Water Electrolyzer. *J. Electrochem. Soc.* *167*, 084509. 10.1149/1945-7111/ab8c89.
25. Panchenko, O., Borgardt, E., Zwaygardt, W., Hackemüller, F.J., Bram, M., Kardjilov, N., Arlt, T., Manke, I., Müller, M., Stolten, D., et al. (2018). In-situ two-phase flow investigation of different porous transport layer for a polymer electrolyte membrane (PEM) electrolyzer with neutron spectroscopy. *J. Power Sources* *390*, 108–115. 10.1016/j.jpowsour.2018.04.044.
26. Chen, Y., Stelmacovich, G., Mularczyk, A., Parkinson, D., Babu, S.K., Forner-Cuenca, A., Pylypenko, S., and Zenyuk, I. V. (2023). A Viewpoint on X-ray Tomography Imaging in Electrocatalysis. *ACS Catal.* *13*, 10010–10025. 10.1021/acscatal.3c01453.
27. Satjaritanun, P., O'Brien, M., Kulkarni, D., Shimpalee, S., Capuano, C., Ayers, K.E., Danilovic, N., Parkinson, D.Y., and Zenyuk, I. V. (2020). Observation of Preferential Pathways for Oxygen Removal through Porous Transport Layers of Polymer Electrolyte Water Electrolyzers. *iScience* *23*, 101783. 10.1016/j.isci.2020.101783.
28. Lee, C., Lee, J.K., Zhao, B., Fahy, K.F., and Bazylak, A. (2019). Transient Gas Saturation in Porous Transport Layers of Polymer Electrolyte Membrane Electrolyzers. *ECS Meet. Abstr. MA2019-02*, 1753–1753. 10.1149/ma2019-02/37/1753.
29. Koch, S., Disch, J., Kilian, S.K., Han, Y., Metzler, L., Tengattini, A., Helfen, L., Schulz, M., Breitwieser, M., and Vierrath, S. (2022). Water management in anion-exchange membrane water electrolyzers under dry cathode operation. *RSC Adv.* *12*, 20778–20784. 10.1039/d2ra03846c.
30. Renz, S., Arlt, T., Kardjilov, N., Helfen, L., Couture, C., Tengattini, A., Lohmann-Richters, F., and Lehnert, W. (2022). Operando Neutron Radiography Measurements of a Zero-Gap Alkaline Electrolysis Cell. *ECS Meet. Abstr. MA2022-02*, 1448–1448. 10.1149/ma2022-02391448mtgabs.
31. Maier, M., Dodwell, J., Ziesche, R., Tan, C., Heenan, T., Majasan, J., Kardjilov, N., Markötter, H., Manke, I., Castanheira, L., et al. (2020). Mass transport in polymer electrolyte membrane water electrolyser liquid-gas diffusion layers: A combined neutron imaging and X-ray computed tomography study. *J. Power Sources* *455*. 10.1016/j.jpowsour.2020.227968.

32. Selamet, O.F., Pasaogullari, U., Spornjak, D., Hussey, D.S., Jacobson, D.L., and Mat, M. (2011). In Situ Two-Phase Flow Investigation of Proton Exchange Membrane (PEM) Electrolyzer by Simultaneous Optical and Neutron Imaging. ECS Meet. Abstr. *MA2011-02*, 978–978. 10.1149/ma2011-02/16/978.
33. J. H. Hubbell, and S. M. Seltzer (2004). X-Ray Mass Attenuation Coefficients. NIST Stand. Ref. Database 126. <https://www.nist.gov/pml/x-ray-mass-attenuation-coefficients>.
34. Kardjilov, N., Fiori, F., Giunta, G., Hilger, A., Rustichelli, F., Strobl, M., Banhart, J., and Triolo, R. (2006). Neutron tomography for archaeological investigations. *J. Neutron Res.* *14*, 29–36. 10.1080/10238160600673201.
35. De Angelis, S., Schuler, T., Charalambous, M.A., Marone, F., Schmidt, T.J., and Büchi, F.N. (2021). Unraveling two-phase transport in porous transport layer materials for polymer electrolyte water electrolysis. *J. Mater. Chem. A* *9*, 22102–22113. 10.1039/d1ta03379d.
36. Maier, M., Owen, R.E., Pham, M.T.M., Dodwell, J., Majasan, J., Robinson, J.B., Hinds, G., Shearing, P.R., and Brett, D.J.L. (2021). Acoustic time-of-flight imaging of polymer electrolyte membrane water electrolyzers to probe internal structure and flow characteristics. *Int. J. Hydrogen Energy* *46*, 11523–11535. 10.1016/j.ijhydene.2021.01.077.
37. Maeв, R.G. (2008). *Acoustic Microscopy: Fundamentals and Applications* (WILEY-VCH Verlag GmbH & Co. KGaA) 10.1002/9783527623136.
38. Dou, Z., Fang, B., Tropf, L., Hoster, H., Schmidt, H., Czarske, J., and Weik, D. (2023). A Water Monitoring System for Proton Exchange Membrane Fuel Cells Based on Ultrasonic Lamb Waves: An Ex Situ Proof of Concept. *IEEE Trans. Instrum. Meas.* *72*, 1–12. 10.1109/tim.2023.3329101.
39. Bertocci, F., Grandoni, A., and Djuric-Rissner, T. (2019). Scanning acoustic microscopy (SAM): A robust method for defect detection during the manufacturing process of ultrasound probes for medical imaging. *Sensors (Switzerland)* *19*, 1–19. 10.3390/s19224868.
40. Yu, H. (2020). Scanning acoustic microscopy for material evaluation. *Appl. Microsc.* *50*. 10.1186/s42649-020-00045-4.
41. Miura, K. (2022). Stiffness reduction and collagenase resistance of aging lungs measured using scanning acoustic microscopy. *PLoS One* *17*, 1–17. 10.1371/journal.pone.0263926.
42. Wasylowski, D., Neubauer, S., Faber, M., Ditler, H., Sonnet, M., Blömeke, A., Dechent, P., Gitis, A., and Sauer, D.U. (2023). In situ tomography of lithium-ion battery cells enabled by scanning acoustic imaging. *J. Power Sources* *580*, 233295. 10.1016/j.jpowsour.2023.233295.
43. Zschach, L.G., Baumann, R., Soldera, F., Méndez, C.M., Apelt, S., Bergmann, U., and Lasagni, A.F. (2023). On the Corrosion Properties of Aluminum 2024 Laser-Textured Surfaces with Superhydrophilic and Superhydrophobic Wettability States. *Adv. Mater. Interfaces* *10*. 10.1002/admi.202300607.
44. Wenzel, R.N. (1936). Resistance Of Solid Surfaces to Wetting by Water. *Eng. Chem.*, 988–994. 10.1017/cbo9781316146743.
45. Wang, Z., Elimelech, M., and Lin, S. (2016). Environmental Applications of Interfacial Materials with Special Wettability. *Environ. Sci. Technol.* *50*, 2132–2150. 10.1021/acs.est.5b04351.
46. Kasem, K.K., and Jones, S. (2008). Platinum as a reference electrode in electrochemical measurements. *Platin. Met. Rev.* *52*, 100–106. 10.1595/147106708X297855.
47. Iwata, R., Zhang, L., Wilke, K.L., Gong, S., He, M., Gallant, B.M., and Wang, E.N. (2021). Bubble growth and departure modes on wettable/non-wettable porous foams in alkaline water splitting. *Joule* *5*, 887–900. 10.1016/j.joule.2021.02.015.
48. Hübschen, G. (2016). Ultrasonic Techniques for Materials Characterization. In *Materials Characterization Using Nondestructive Evaluation (NDE) Methods* (Elsevier Ltd), pp. 177–234. 10.1016/B978-0-08-

100040-3.00006-7.

49. Baskota, A., Kuo, J., Ardanuc, S., and Lal, A. (2023). Characterization of cells and tissues using a compact GHz ultrasonic imager. *IEEE Int. Ultrason. Symp. IUS*, 16–19. 10.1109/IUS51837.2023.10307657.
50. Zhao, X., Ren, H., and Luo, L. (2019). Gas Bubbles in Electrochemical Gas Evolution Reactions. *Langmuir* 35, 5392–5408. 10.1021/acs.langmuir.9b00119.
51. Chatzis, I., Morrow, N.R., and Lim, H.T. (1983). Magnitude and Detailed Structure of Residual Oil Saturation. *Soc. Pet. Eng. J.* 23, 311–326. 10.2118/10681-PA.
52. Lenormand, R., Touboul, E., and Zarcone, C. (1988). Numerical models and experiments on immiscible displacements in porous media. *J. Fluid Mech.* 189, 165–187. 10.1017/S0022112088000953.
53. Assael, M.J., Kalyva, A.E., Monogenidou, S.A., Huber, M.L., Perkins, R.A., Friend, D.G., and May, E.F. (2018). Reference Values and Reference Correlations for the Thermal Conductivity and Viscosity of Fluids. *J. Phys. Chem. Ref. Data* 47, 1–23. 10.1063/1.5036625.
54. Hauner, I.M., Deblais, A., Beattie, J.K., Kellay, H., and Bonn, D. (2017). The Dynamic Surface Tension of Water. *J. Phys. Chem. Lett.* 8, 1599–1603. 10.1021/acs.jpcclett.7b00267.
55. Kestin, J., Sokolov, M., and Wakeham, W.A. (1978). Viscosity of Liquid Water in the Range -8 °C to 150 °C. *J. Phys. Chem. Ref. Data* 7, 941–948.
56. Hughes, R.G., and Blunt, M.J. (2000). Pore scale modeling of rate effects in imbibition. *Transp. Porous Media* 40, 295–322. 10.1023/A:1006629019153.
57. Joekar-Niasar, V., and Hassanizadeh, S.M. (2012). Analysis of fundamentals of two-phase flow in porous media using dynamic pore-network models: A review. *Crit. Rev. Environ. Sci. Technol.* 42, 1895–1976. 10.1080/10643389.2011.574101.
58. Tiab, D., and Donaldson, E.C. (2011). Petrophysics: Theory and Practice of Measuring Reservoir Rock and Fluid Transport Properties. In *Petrophysics* (Elsevier Inc.), pp. 375–377. 10.1016/C2009-0-64503-7.
59. Schneider, C.A., Rasband, W.S., and Eliceiri, K.W. (2012). NIH Image to ImageJ: 25 years of image analysis. *Nat. Methods* 9, 671–675. 10.1038/nmeth.2089.
60. PVA TePla Scanning Acoustic Microscopy SAM Premium Line <https://www.pvatepla-sam.com/en/products/sam-premium-line/>.
61. Weik, D., Dou, Z., Rübiger, D., Vogt, T., Eckert, S., Czarske, J., and Büttner, L. (2024). Uncertainty Quantification of Super-Resolution Flow Mapping in Liquid Metals using Ultrasound Localization Microscopy. 10.48550/arXiv.2404.10840.

## Supplemental information

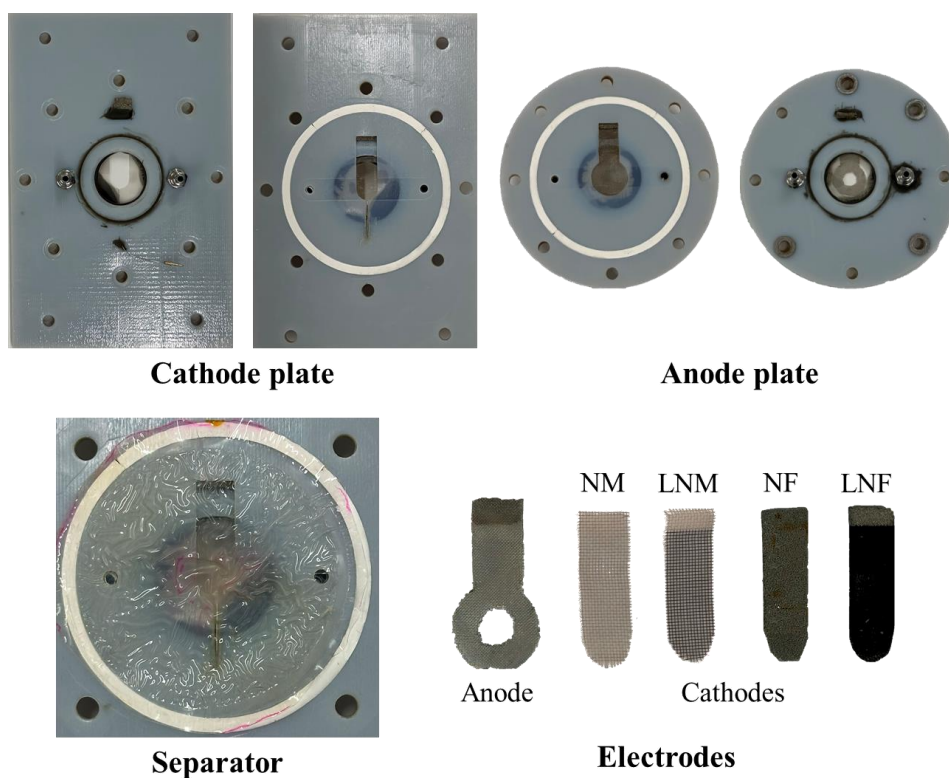


**Figure S1.** Images of the parts of the bespoke AWE, the ring shape counter electrode (anode) and the four investigated cathodic electrodes.

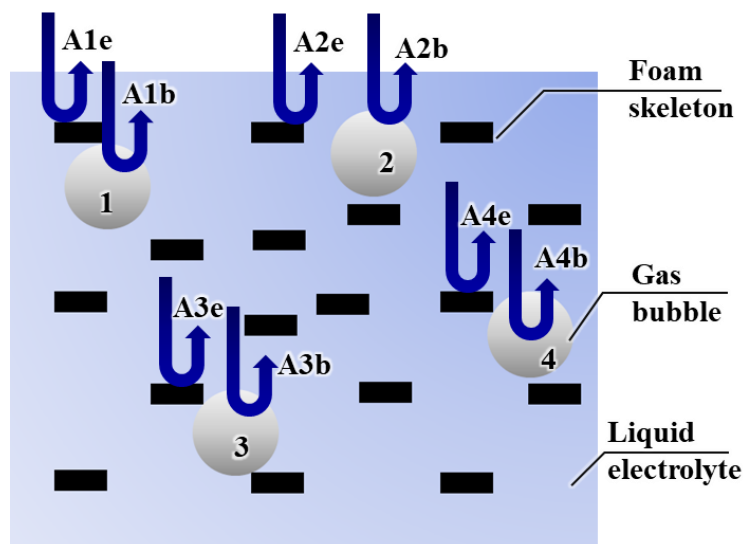


**Figure S2.** The complicated diffractive scattering of ultrasonic waves in the open cell foam structures resulted to unpredictable relations of echo intensities from electrode and bubbles. For instance, at shallower positions, we may have  $A1e \approx A1b$  and  $A2e < A2b$ . However, due to the irregular geometry of the foam skeleton, we are not able to determine the relations of  $A3e$  and  $A3b$ , as well as  $A4e$  and  $A4b$ . This led us to use a subtraction-based image processing scheme for isolating the produced bubbles from the NF and LNF.

NM @  $|j_{geo}| = 40 \text{ mA/cm}^2$

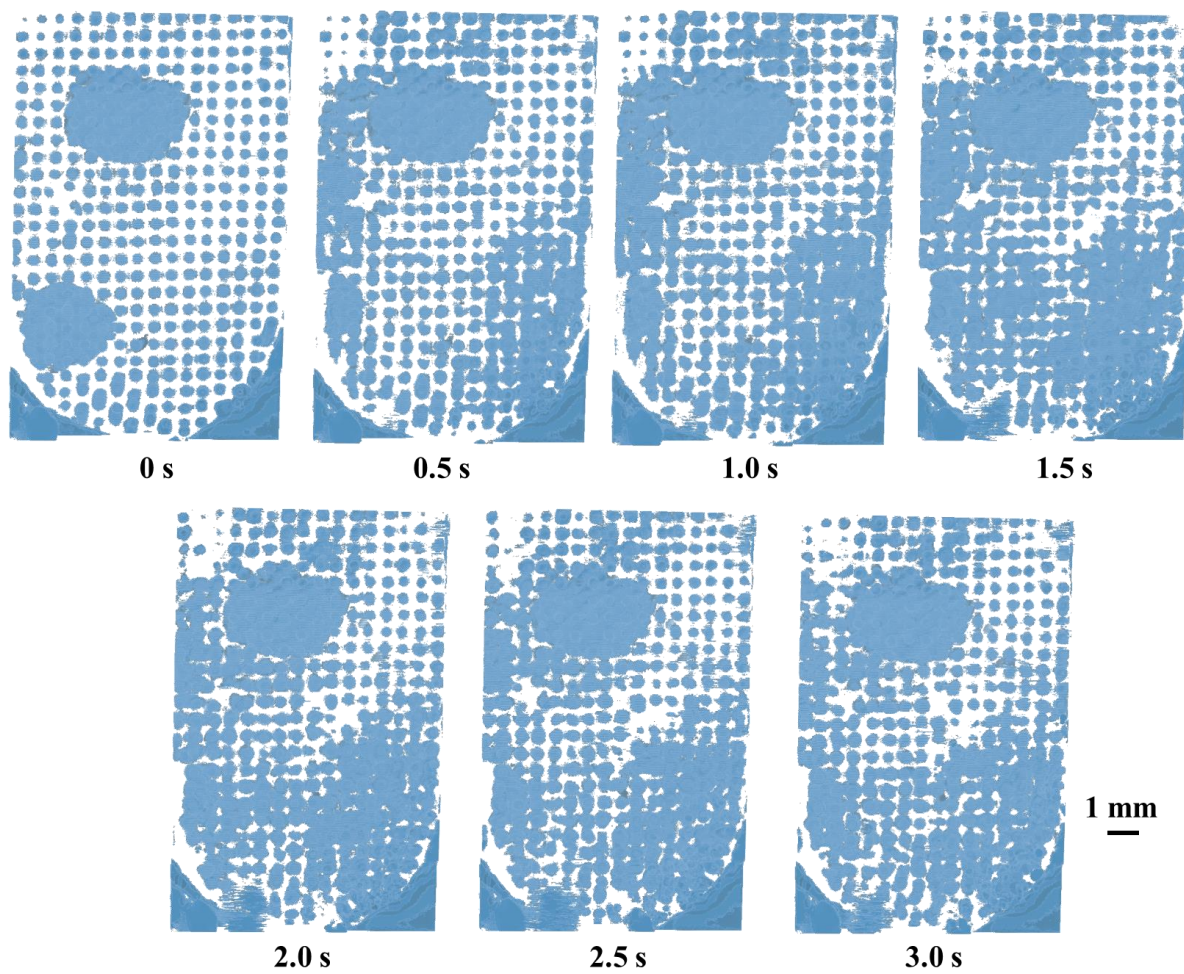


**Figure S3.** Time lapse images of the bubbles attached to the NM at the current density of  $40 \text{ mA/cm}^2$  and without the flow-by condition.

LNM @  $|j_{geo}| = 40 \text{ mA/cm}^2$

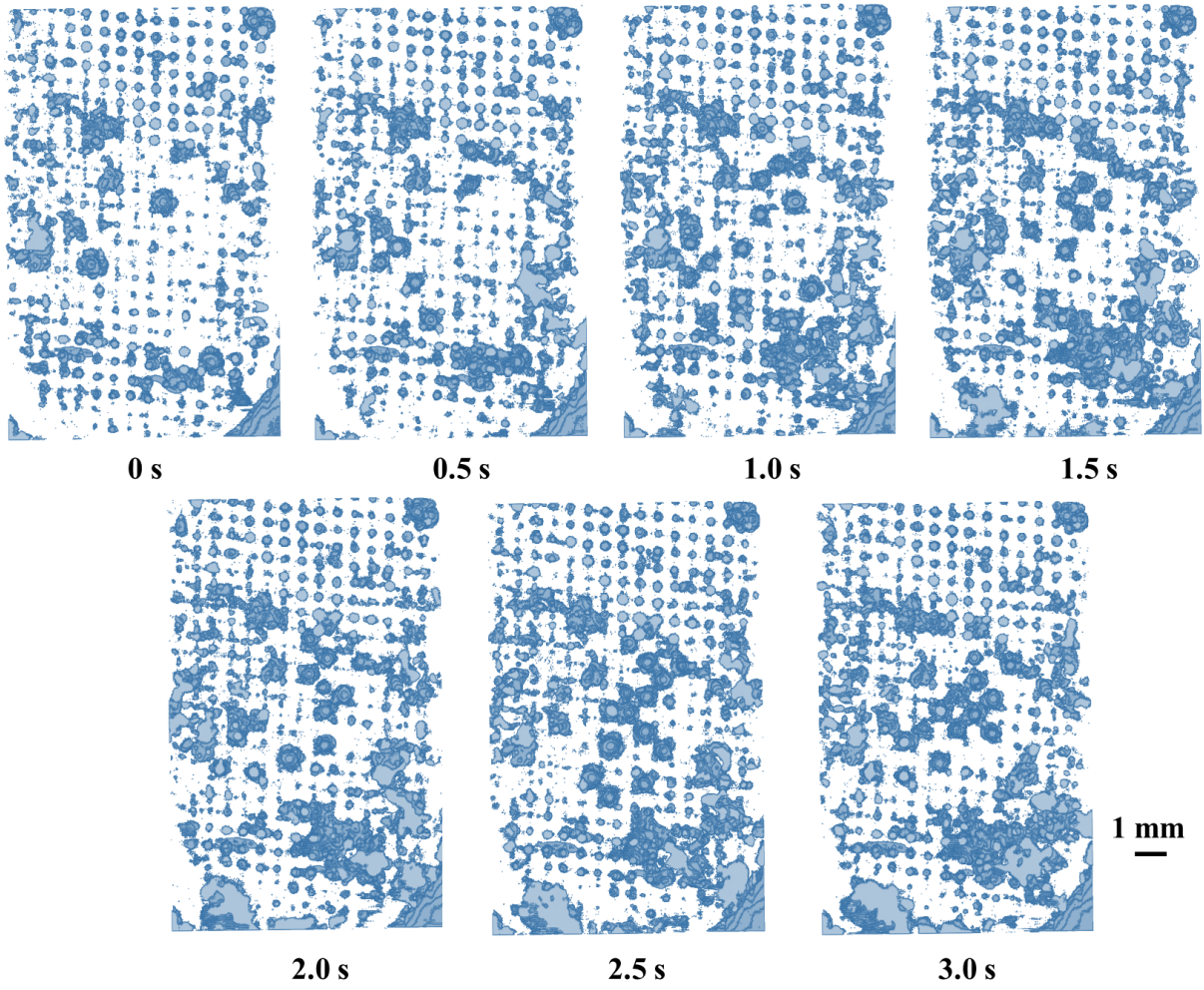


**Figure S4.** Time lapse images of the bubbles attached to the LNM at the current density of  $40 \text{ mA/cm}^2$  and without the flow-by condition.

LNM @  $|j_{geo}| = 80 \text{ mA/cm}^2$

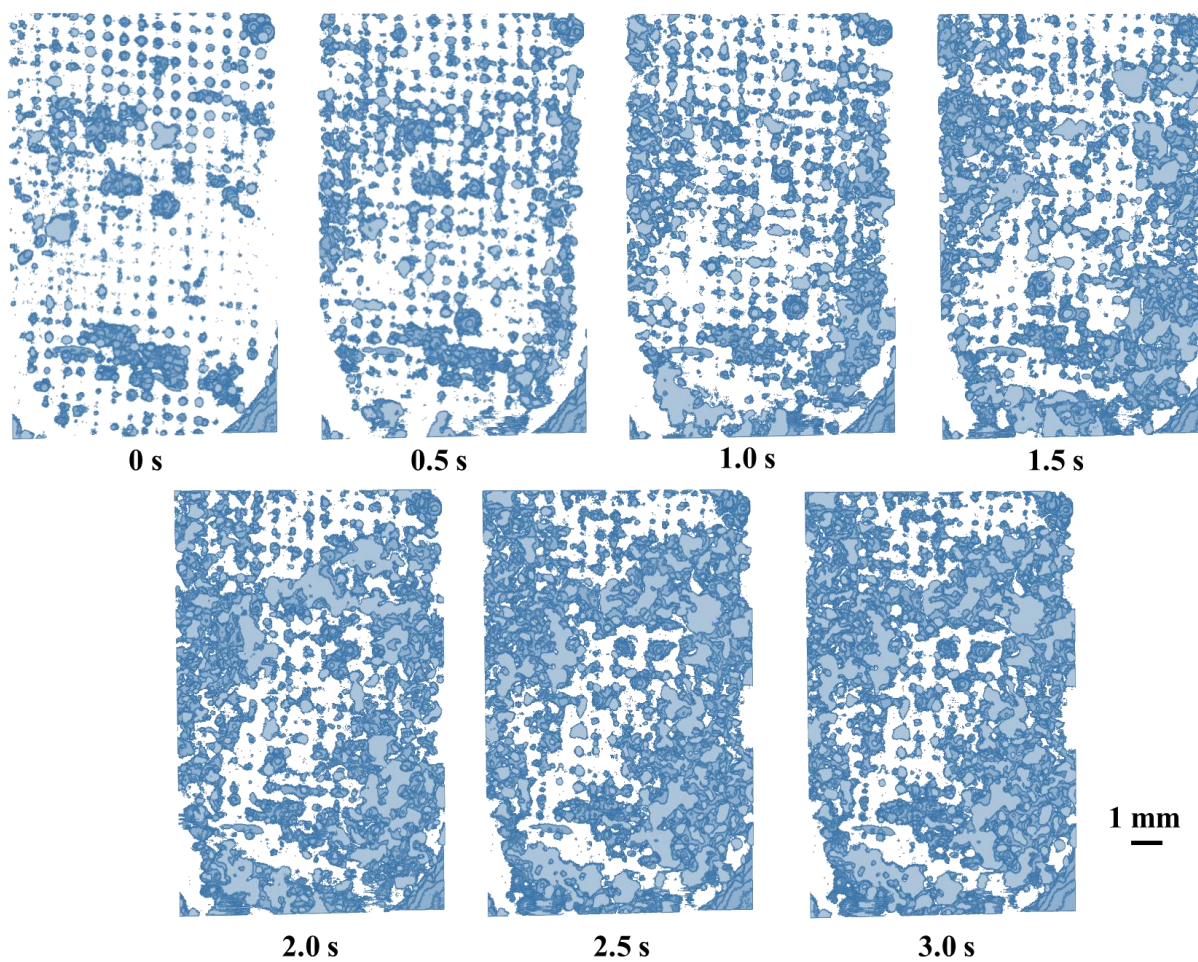


**Figure S5.** Time lapse images of the bubbles attached to the LNM at the current density of  $80 \text{ mA/cm}^2$  and without the flow-by condition.

LNM @  $|j_{geo}| = 80 \text{ mA/cm}^2$  with flow-by

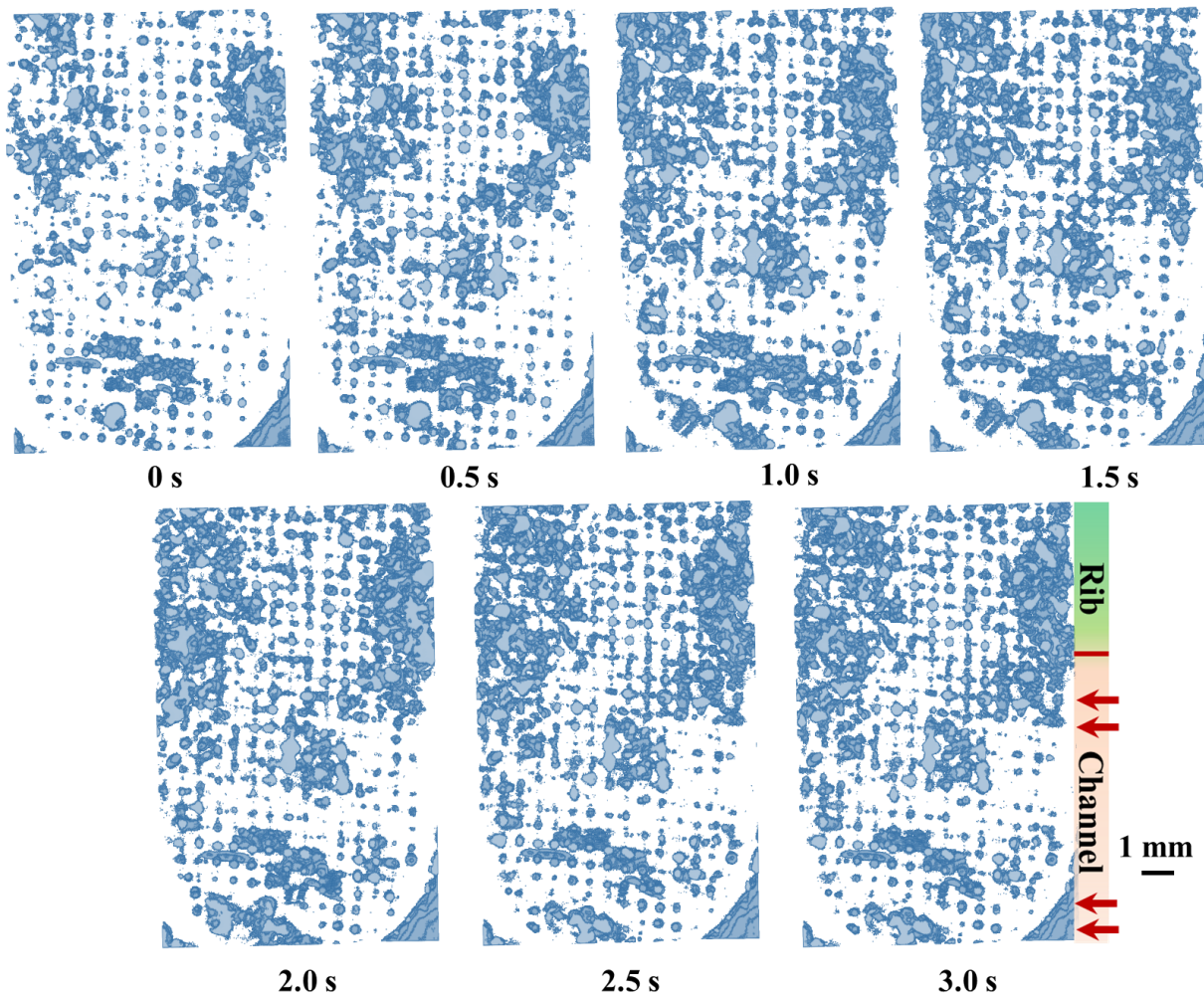


**Figure S6.** Time lapse images of the bubbles attached to the LNM at the current density of  $80 \text{ mA/cm}^2$  and with the flow-by condition. The positions of the channel and the rib are given as well. The red arrows show the flow-by direction.

NF @  $|j_{geo}| = 80 \text{ mA/cm}^2$

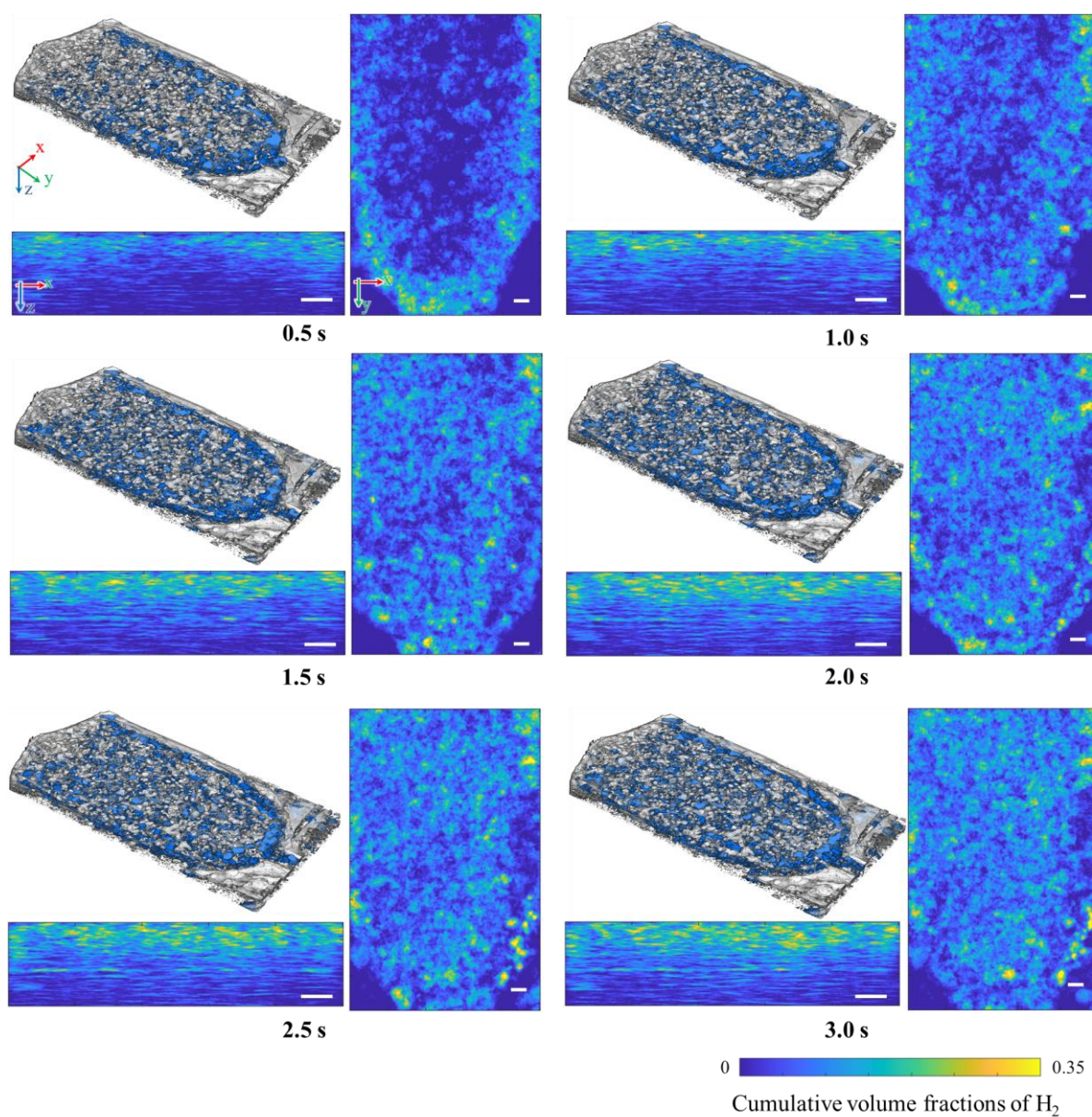


**Figure S7.** Time lapse images of the volume fraction of produced bubbles in the NF at the current density of  $80 \text{ mA/cm}^2$  and without the flow-by condition. Scale bar is 1 mm.

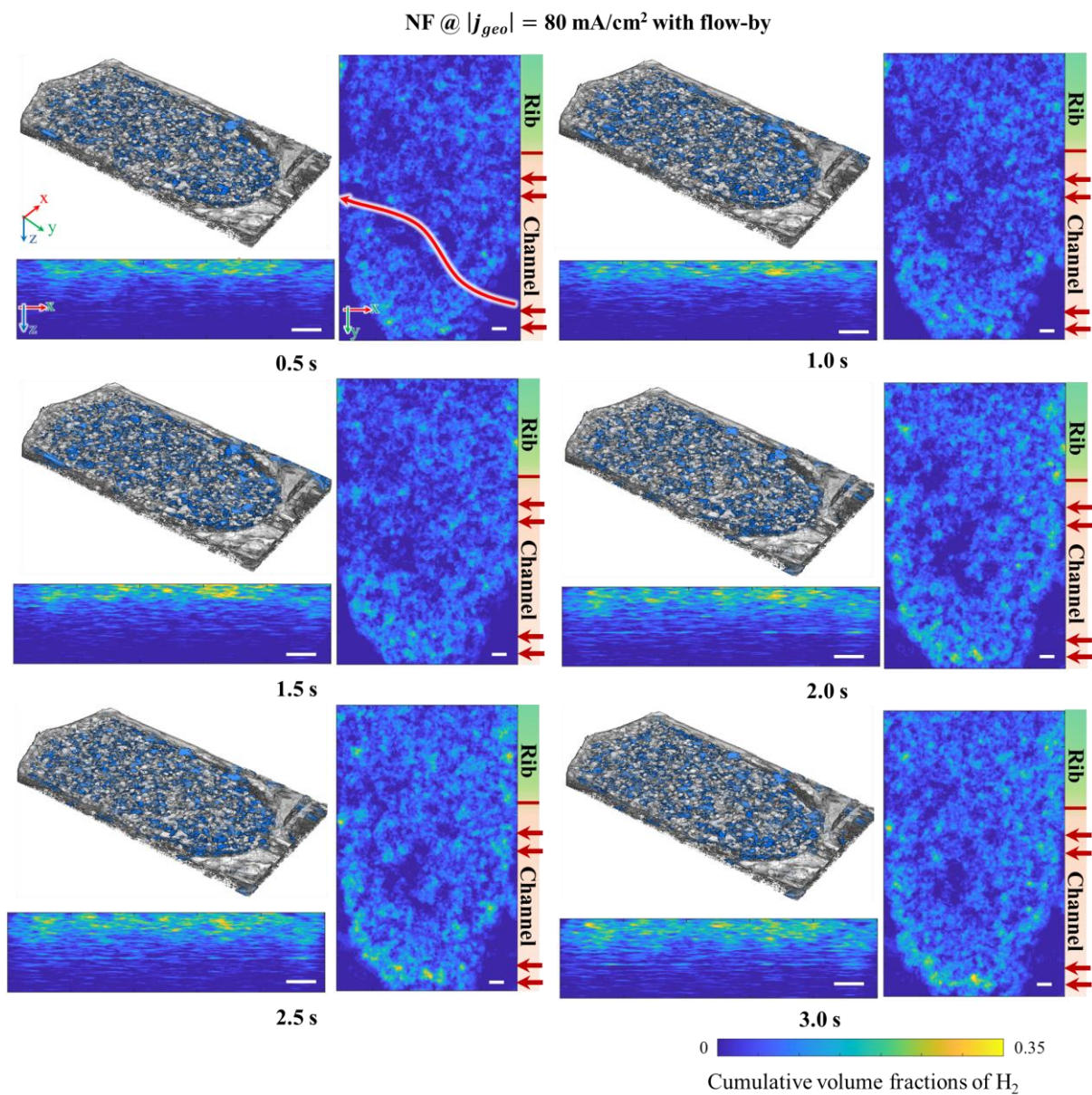


**Figure S8.** Time lapse images of the volume fraction of produced bubbles in the NF at the current density of  $80 \text{ mA/cm}^2$  and with the flow-by condition. Scale bar is  $1 \text{ mm}$ . The positions of the channel and the rib are given as well. The red arrows show the flow-by direction. The low-resistance electrolyte pathway is more clearly observed as in the middle of the NF marked by the red arrow.

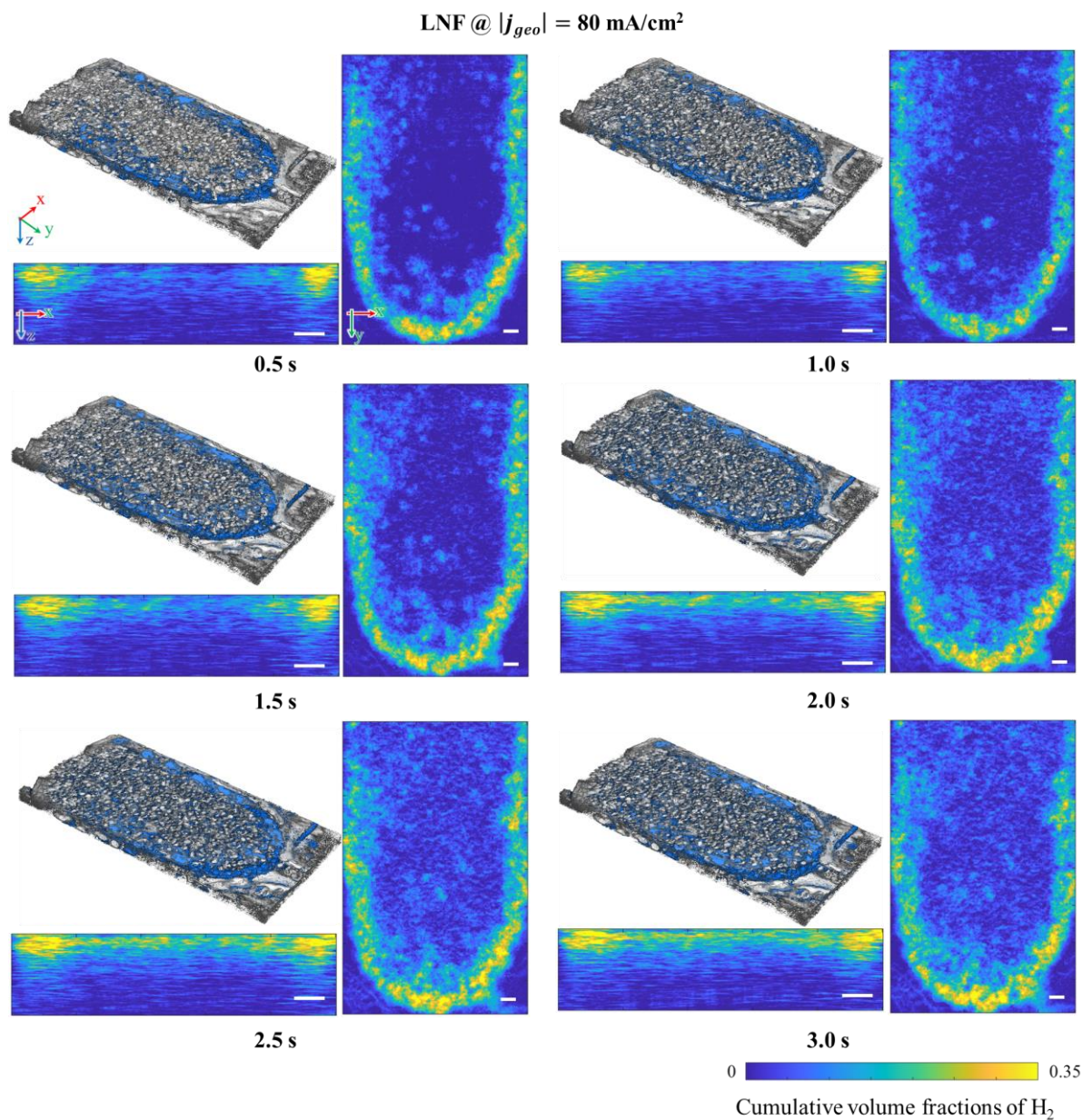


**Figure S9.** Time lapse images of the volume fraction of produced bubbles in the LNF at the current density of  $80 \text{ mA/cm}^2$  and without the flow-by condition. Scale bar is 1 mm.

LNF @  $|j_{geo}| = 80 \text{ mA/cm}^2$  with flow-by

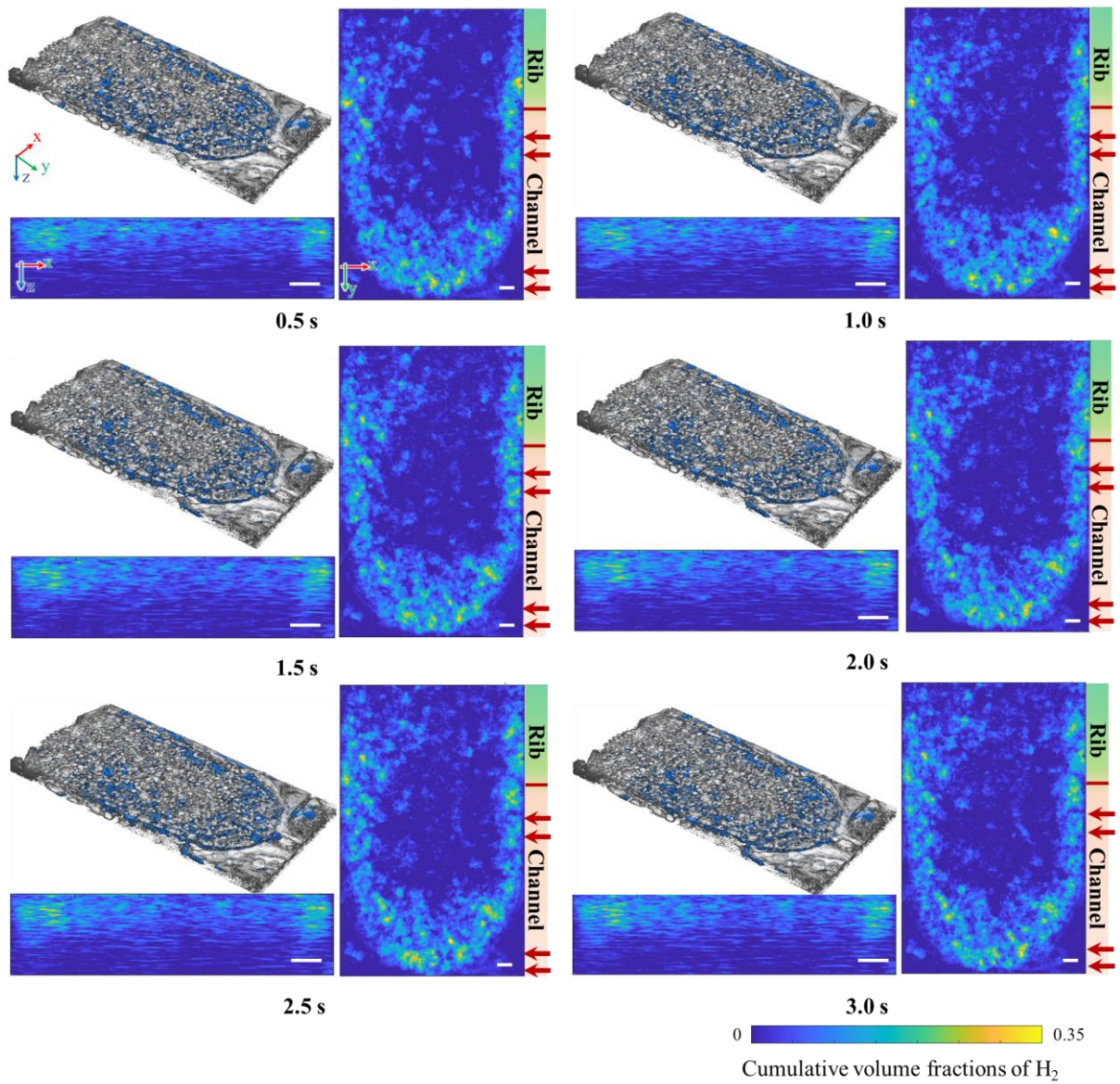


**Figure S10.** Time lapse images of the volume fraction of produced bubbles in the LNF at the current density of 80 mA/cm<sup>2</sup> and with the flow-by condition. Scale bar is 1 mm. The positions of the channel and the rib are given as well.

### Note S1. Modelling of ultrasound beam profile in the AWE environment

We model the beam profile of the ultrasonic transducer used in our experiments.

The depth of focus (DoF) of the transducer is calculated as (1),<sup>1</sup> in which  $\lambda$  is the spatial pulse length in the electrolyte (see **Table S1** for the speed of sound), corresponding to a mid-frequency of 75 MHz. D and F are the diameter and focal length of the acoustic lens (see **Figure 2B** in the main text), which are 6 mm and 20 mm, respectively. The slight deflection due to ultrasound transmitting through PMMA is neglected.

$$\text{DoF} = 7\lambda \left(\frac{F}{D}\right)^2 = 7 \cdot \frac{1580 \frac{m}{s}}{75 \cdot 10^6 \text{ Hz}} \cdot \left(\frac{20 \text{ mm}}{6 \text{ mm}}\right)^2 = 1.64 \text{ mm} \quad (1)$$

The beam diameter of the transducer is given in (2), which is equivalent to the lateral resolution. The theoretical value is in good agreement with the actual measured result of approx. 68  $\mu\text{m}$ .

$$r_l \approx \frac{\lambda}{2 \cdot NA} = \frac{\lambda}{2 \cdot \left(\frac{D}{2F}\right)} = \frac{\lambda \cdot F}{D} = 70.2 \mu\text{m} \quad (2)$$

The axial resolution is known as half of the spatial length of the excited ultrasound pulse, as given in (3).

$$r_a \approx \frac{\lambda}{2} = 10.5 \mu\text{m} \quad (3)$$

**Table S1. Acoustic properties of different materials of the AWE**

<b>Materials</b>	<b>In AWE</b>	<b>Density (Kg/m<sup>3</sup>)</b>	<b>Speed of sound (m/s)</b>	<b>Acoustic impedance (Mrayl/m<sup>2</sup>)<sup>b</sup></b>
Pure water	Coupling agent	1000	1450	1.45
PMMA <sup>2</sup>	Flow filed plate (electrode region)	1180	2730	3.19
SLA resin <sup>a</sup>	Flow filed plate	1100 - 1300	2350	2.59 – 3.06
Epoxy <sup>3</sup>	Jointing PMMA and SLA resin	1070	~ 2000	2.14
8 wt% KOH solution <sup>a</sup>	Electrolyte	1069	1580	1.69
Ni <sup>c,4</sup>	Electrode	8900	6040	53.76
Air	Bubbles	1.293	340	0.44

<sup>a</sup> Experimental determined in this work.

<sup>b</sup> The reflection coefficients at different phase interfaces can be estimated from the acoustic impedance mismatch.

<sup>c</sup> Note that these listed values are for pure Ni but not the porous Ni electrodes.

## References

1. Younan, Y., Jean-francois, A., and Mickael, T. (2014). Non-invasive therapy of brain disorders with focused ultrasound: from animal experiments to clinical transfer. Thesis. Université Pierre et Marie Curie - Paris VI
2. Xia, W., Piras, D., van Hespén, J.C.G., Steenbergen, W., and Manohar, S. (2013). A new acoustic lens material for large area detectors in photoacoustic breast tomography. *Photoacoustics 1*, 9–18. 10.1016/j.pacs.2013.05.001.
3. Suñol, F., Ochoa, D.A., Granados, M., González-Cinca, R., and García, J.E. (2020). Performance Assessment of Ultrasonic Waves for Bubble Control in Cryogenic Fuel Tanks. *Microgravity Sci. Technol. 32*, 609–613. 10.1007/s12217-020-09795-y.
4. Solids and Metals - Speed of Sound [https://www.engineeringtoolbox.com/sound-speed-solids-d\\_713.html](https://www.engineeringtoolbox.com/sound-speed-solids-d_713.html). Accessed on 2023.10.30.